

X-Ray Detection of the Galaxy’s Missing Baryons in the Circum-Galactic Medium of L* Galaxies

FABRIZIO NICASTRO,^{1,2} Y. KRONGOLD,³ T. FANG,² F. FRATERNALI,⁴ S. MATHUR,^{5,6} S. BIANCHI,⁷ A. DE ROSA,⁸
E. PICONCELLI,¹ L. ZAPPACOSTA,¹ M. BISCHETTI,^{9,10} C. FERUGLIO,⁹ AND A. GUPTA^{5,11}

¹*Istituto Nazionale di Astrofisica (INAF) - Osservatorio Astronomico di Roma
Via Frascati 33*

00078 Monte Porzio Catone (RM), Italy

²*Department of Astronomy, Xiamen University, Xiamen, Fujian 361005, China*

³*Instituto de Astronomia - Universidad Nacional Autonoma de Mexico, Mexico City, Mexico*

⁴*Kapteyn Astronomical Institute, University of Gronigen, Gronigen, The Netherlands*

⁵*Astronomy Department, The Ohio State University, Columbus, OH, USA*

⁶*Center for Cosmology and Astro-Particle Physics, The Ohio State University, Columbus, OH, USA*

⁷*Dipartimento di Matematica e Fisica, Università degli Studi Roma Tre, Roma, Italy*

⁸*Istituto Nazionale di Astrofisica (INAF) - Istituto di Astrofisica e Planetologia Spaziali, Roma, Italy*

⁹*Istituto Nazionale di Astrofisica (INAF) - Osservatorio Astronomico di Trieste, Trieste, Italy*

¹⁰*Dipartimento di Fisica, Sezione di Astronomia, Università di Trieste, Trieste, Italy*

¹¹*Columbus State Community College, Columbus, OH, USA*

ABSTRACT

The amount of baryons hosted in the disks of galaxies is lower than expected based on the mass of their dark-matter halos and the fraction of baryon-to-total matter in the universe, giving rise to the so called galaxy missing-baryon problem. The presence of cool circum-galactic matter gravitationally bound to its galaxy’s halo up to distances of at least ten times the size of the galaxy’s disk, mitigates the problem but is far from being sufficient for its solution. It has instead been suggested, that the galaxy missing baryons may hide in a much hotter gaseous phase of the circum-galactic medium, possibly near the halo virial temperature and co-existing with the cool phase. Here we exploit the best available X-ray spectra of known cool circum-galactic absorbers of L* galaxies to report the first direct high-statistical-significance ($5.3 - 6.2\sigma$) detection of associated O VII and N VI absorption in the stacked *XMM-Newton* and *Chandra* spectra of three quasars. We show that these absorbers trace hot medium in the X-ray halo of these systems, at $\log T(\text{in K}) \simeq 5.73 - 6.4$ K (comprising the halo virial temperature $T_{\text{vir}} = 10^6$ K). We estimate a mass of the X-ray halo within 1 virial radius $M_{\text{hot-CGM}} \simeq (0.6 - 3) \times 10^{11} (Z/0.3Z_{\odot})^{-1} M_{\odot}$, corresponding, for these systems, to a galaxy missing baryon fraction $\xi = M_{\text{hot-CGM}}/M_{\text{missing}} \simeq (0.5 - 2.2)(Z/0.3Z_{\odot})^{-1}$ and thus potentially closing the galaxy baryon census in typical L* galaxies. Our measurements contribute significantly to the solution of the long-standing galaxy missing baryon problem and to the understanding of the continuous cycle of baryons in-and-out of galaxies throughout the life of the universe.

Keywords: Circumgalactic medium (1879) — Galaxies (573) — Galaxy evolution (594) — X-ray quasars (1821) — High resolution spectroscopy (2096)

1. INTRODUCTION

The galaxy missing baryon problem is present at all halo scales, from dwarves to massive elliptical galaxies and up to groups and clusters of galaxies (e.g. [McGaugh et al. \(2010\)](#)) but the baryon deficit is larger for smaller halos. Galaxy disks in halos of $10^{12} M_{\odot}$ host only $\sim 20\%$ of the expected baryons ([McGaugh et al. 2010](#)). However, due to their

non-baryonic massive halos, the gravitational pull of galaxies extends well beyond their stellar disks, up to distances of at least ten times their size.

Such large volumes of space surrounding the stellar disks are not empty but are known to host clouds of cool ($T \simeq 10^4$ K) gas, gravitationally bound to the galaxy. As suggested by the extensive studies carried out, for the local universe, in the Far-ultraviolet band ($\sim 900 - 2000 \text{ \AA}$, FUV, hereinafter) with the Hubble Cosmic Origin Spectrograph (COS, McPhate et al. (2000)), this cool circum-galactic matter (cool-CGM, hereinafter) may be in photoionization equilibrium with the external meta-galactic UV radiation field in which is embedded (e.g. Berg et al. (2023); Lehner et al. (2019); Berg et al. (2019); Wotta et al. (2019); Lehner et al. (2018); Keeney et al. (2017); Werk et al. (2014); Fox et al. (2013); Lehner et al. (2013); Werk et al. (2013); Stocke et al. (2013), but see also Bregman et al. (2018) and references therein for alternative possibilities), and often co-exists with higher-ionization gas in a different physical state, probed by Li-like ions of oxygen (e.g. Stocke et al. (2013); Tchernyshyov et al. (2022); Prochaska et al. (2019, 2011)) and/or neon (e.g. Burchett et al. (2019)). Under the pure-photoionization equilibrium hypothesis, the cool-CGM may contribute importantly to the galaxy baryon budget: for typical L^* galaxies¹ with halo mass of $1.6 \times 10^{12} M_\odot$ and a factor of 4 deficit of baryons (e.g. McGaugh et al. (2010)), it may account for up to 50% of the missing baryonic matter (Werk et al. (2014), but see also Bregman et al. (2018)).

At least 50% of the galaxy missing baryons, however, remains elusive, and is thought to hide in a hotter phase of the CGM (Wijers et al. 2020), possibly at the galaxy virial temperature (i.e. $T_{vir} \simeq 10^{5.7-6.0}$ K, for halo masses of $M_h \simeq 10^{11.8-12.3} M_\odot$ at $z = 0$, e.g. Qu & Bregman (2018)). Observationally, the presence of this hot phase is currently only hinted through Sunyaev-Zeldovich (Bregman et al. 2022) and low-resolution X-ray (Das et al. 2020) measurements of the surroundings of local L^* galaxy or pioneering X-ray absorption (Mathur et al. 2021) studies (see below), and more ubiquitously through absorption by moderately-ionized ions of oxygen (e.g. Stocke et al. (2013); Tchernyshyov et al. (2022); Prochaska et al. (2019, 2011)) and neon (e.g. Burchett et al. (2019)). At such high temperatures, indeed, hydrogen is virtually fully ionized and so difficult to detect. Therefore, the only available tracers (with typical ion fractions of only a few percent) in the FUV portion of the electromagnetic spectrum are the Li-like ions of oxygen (at $z \leq 0.7$) and neon (at $z \simeq 0.2-1.3$). However, Li-like ions in the CGM may be produced either in tenuous warm clouds purely photo-ionized by the external radiation field or in much hotter, mainly collisionally-ionized, gas (see §F). Distinguishing between these two possibilities is virtually impossible based on the currently available single ion column density measurements (i.e. without estimates of the gas ionization balance) and thus only loose lower limits on the temperature and mass contribution of this gaseous CGM component have been set so far (e.g. Tumlinson et al. (2011); Chen & Prochaska (2000)).

Better tracers of gas at $T \simeq 10^6$ K, are the He-like ions of oxygen and nitrogen, which represent about 90% of their elements in $T \simeq 10^{5.6-6.2}$ K gas in collisional-ionization equilibrium (CIE; see §F), and whose main transitions lie in the soft X-ray band. Pioneering single-target X-ray spectroscopic studies of these transitions from the halos of optimally-selected Lyman-Limit-Systems (low-ionization HI-metal absorbers with moderate column density: $16.2 \leq \log N_{HI}(\text{in cm}^{-2}) \leq 19$; LLSs, hereinafter) have indeed been recently performed (Mathur et al. 2021), but are hampered by the limited resolution and throughput of current X-ray spectrometers, and did not produce conclusive results. Detailed surveys of galaxy—high-ionization X-ray-absorber associations, comparable to low- or moderate-ionization FUV studies like the COS-Halos Survey (Werk et al. 2013) or the CGM2 Survey (Tchernyshyov et al. 2022), will have to wait for the next generation of high-throughput X-ray spectrometers (e.g. the Athena-XIFU Barret et al. (2018) or Arcus Smith (2020); Wijers et al. (2020)). In the meantime, exploiting the richness of the Chandra-LETG (Low Energy Transmission Grating, Brinkman et al. (2000)) and XMM-Newton RGS (Reflection Grating Spectrometers, den Herder et al. (2000)) archives and adopting “stacking” techniques (e.g. Kovács et al. (2019), Ahoranta et al. (2020, 2021)) to perform spectroscopy of optimally selected targets, is a viable alternative.

Previous studies pursued this strategy by using as signposts for the X-ray transitions the average redshifts of groups of intervening galaxies, and reported non-detection of hot-X-ray intra-group gas (Yao et al. 2010). Here, instead, we choose to focus on the redshifts of known intervening cool (LLSs) and warm absorbers already extensively studied in the FUV and on their galaxy-associations.

Throughout the paper, we adopt a standard Λ CDM cosmology, with the latest parameter values from Planck Collaboration et al. (2020) (from the combined analysis of temperature power spectra, high-multipole polarization

¹ L^* is the characteristic luminosity above which the number of galaxies per unit volume drops exponentially and, in the local Universe, corresponds to the luminosity of a Milky-Way-like galaxy.

spectra and lensing). In particular, we use universal baryon fraction $f_b = \Omega_b/\Omega_m = 0.157$. We also adopt solar metallicities from [Anders & Grevesse \(1989\)](#). In particular we use $[N/H]=-3.95$ and $[O/H]=-3.07$. Uncertainties are quoted at 68% significance throughout the paper, unless explicitly stated.

2. SAMPLE SELECTION AND THE X-RAY HALO

We select as optimal targets the 30 background quasars of [Lehner et al. \(2013\)](#) and [Prochaska et al. \(2019\)](#) for which LLSs are reported, often associated with moderate-ionization OVI absorbers ([Fox et al. 2013](#); [Lehner et al. 2013](#)).

Eleven of these objects have *XMM-Newton* RGS data available, and two of these have also *Chandra* -LETG data (see §A). Of these eleven targets, we selected only those (a) whose total RGS and LETG spectra have signal-to-noise per resolution element $SNRE > 4$ in the continuum adjacent the LLS-frame O VII $K\alpha$ transition and (b) whose intervening LLSs have been confidently associated to $\sim L^*$ galaxies.

This yielded three quasars, namely PG 1407+265 (observed only with *XMM-Newton*), PKS 0405-123 and PG 1116+215 (observed with both *XMM-Newton* and *Chandra*), whose lines of sight cross low-ionization LLSs and OVI absorbers at $z_{LLS\#1} = 0.6828$ ([Wotta et al. \(2019\)](#); [Fox et al. \(2013\)](#); [Lehner et al. \(2013\)](#); LLS#1, hereinafter), $z_{LLS\#2} = 0.1671$ ([Wotta et al. \(2019\)](#); [Fox et al. \(2013\)](#); [Lehner et al. \(2013\)](#); [Stocke et al. \(2013\)](#); LLS#2) and $z_{LLS\#3} = 0.1385$ ([Wotta et al. \(2019\)](#); [Fox et al. \(2013\)](#); [Lehner et al. \(2013\)](#); [Stocke et al. \(2013\)](#); LLS#3), respectively (see §A for further details).

The three LLSs that we use to build our X-ray halo, and their galaxy associations, have been reported and discussed in several studies ([Berg et al. 2023](#); [Wotta et al. 2019](#); [Keeney et al. 2017](#); [Fox et al. 2013](#); [Lehner et al. 2013](#); [Werk et al. 2013](#); [Stocke et al. 2013](#); [Burchett et al. 2019](#)) and their properties are reported in Table 2 of §B. They all also have HI column densities close to the lowest threshold $N_{HI} = 10^{16.2} \text{ cm}^{-2}$ of the LLS definition in [Lehner et al. \(2013\)](#) and are seen at impact parameters (i.e. the line-of-sight to galaxy-center projected distance) $\rho > 90$ kpc (Table 2 in §B). This strongly suggests a cool-CGM (and not extended gaseous disk) origin for the HI-metal absorbers observed in these three systems ([Bregman et al. 2018](#)). The three LLSs of our sample have all co-located OVI absorption that, however, in the pure-photoionization hypothesis for the cool-CGM traced by the LLSs, is not entirely physically associated to the cool gas (e.g. [Lehner et al. \(2013\)](#)).

The X-ray halo resulting from the σ_{OVI}^i -weighted averages (see §3 and B) of the properties of the LLSs and galaxy-associations of our sample, is that of an L^* galaxy at $\langle z_{X-ray-halo} \rangle = 0.295$, with a halo mass of $M_h \simeq 1.25 \times 10^{12} M_\odot$ and a virial radius of $R_{vir} \simeq 200$ kpc. The constructed X-ray line of sight intercepts the X-ray halo at a projected distance $\rho = 114$ kpc from its center ($\sim 0.6 R_{vir}$; last row of Table 2 in §B). Assuming a spherical halo with virial radius $R_{vir} = R_{200}$ (the radius at which the halo density equals $200\times$ the universe critical density at the given redshift), the line-of-sight pathlength through the X-ray halo is therefore $L = 2\sqrt{R_{vir}^2 - \rho^2} \simeq 330$ kpc.

3. THE X-RAY HALO SPECTRUM

Table 1 of §A lists the 3 targets of our X-ray-halo sample and the properties of their X-ray spectra. The last row of Table 1 contains the total available X-ray exposure and SNREs (added in quadrature).

3.1. Hints of O VII $K\alpha$ absorption along individual sightlines

We first examined each source X-ray spectrum for a signature of O VII $K\alpha$ absorption (the strongest transition expected in gas at $T \simeq 10^6$ K) at the redshifts of its LLS. We did this by modeling each RGS and LETG spectrum within the fitting-package Sherpa (part of the *Ciao* software [Fruscione et al. \(2006\)](#)) with a simple power-law plus Galactic absorption model. The five spectra of our three targets, blueshifted to their X-ray-LLS redshifts (see below) for easy comparison, together with their best-fitting continua (solid curves) are shown in Fig. 1. None of the single-source spectra shows the clear presence of a possible O VII $K\alpha$ absorption line imprinted by the halo of the intervening galaxies (i.e. at $\lambda = 21.6 \text{ \AA}$ in Fig. 1), but all of them are consistent with the presence of such a feature at a statistical significance level of $\sim 1-2\sigma$. Figures 7-9, in §C, show the confidence-level contours of the O VII $K\alpha$ line flux and centroid hinted in the *XMM-Newton* -RGS and *Chandra* -LETG spectra of our three targets.

The line hinted in the LETG spectrum of PKS 0405-123 was already reported by our group [Mathur et al. \(2021\)](#) at the level of statistical significance shown also here in Fig. 8 ($\sim 2\sigma$), and modeled as the hot counterpart of LLS#2 in association with the OVI absorber reported by [Savage et al. \(2010\)](#). However, the statistical significance of this line alone did not allow us to reach definitive conclusions on the temperature, column density and mass of this hot-CGM absorber [Mathur et al. \(2021\)](#).

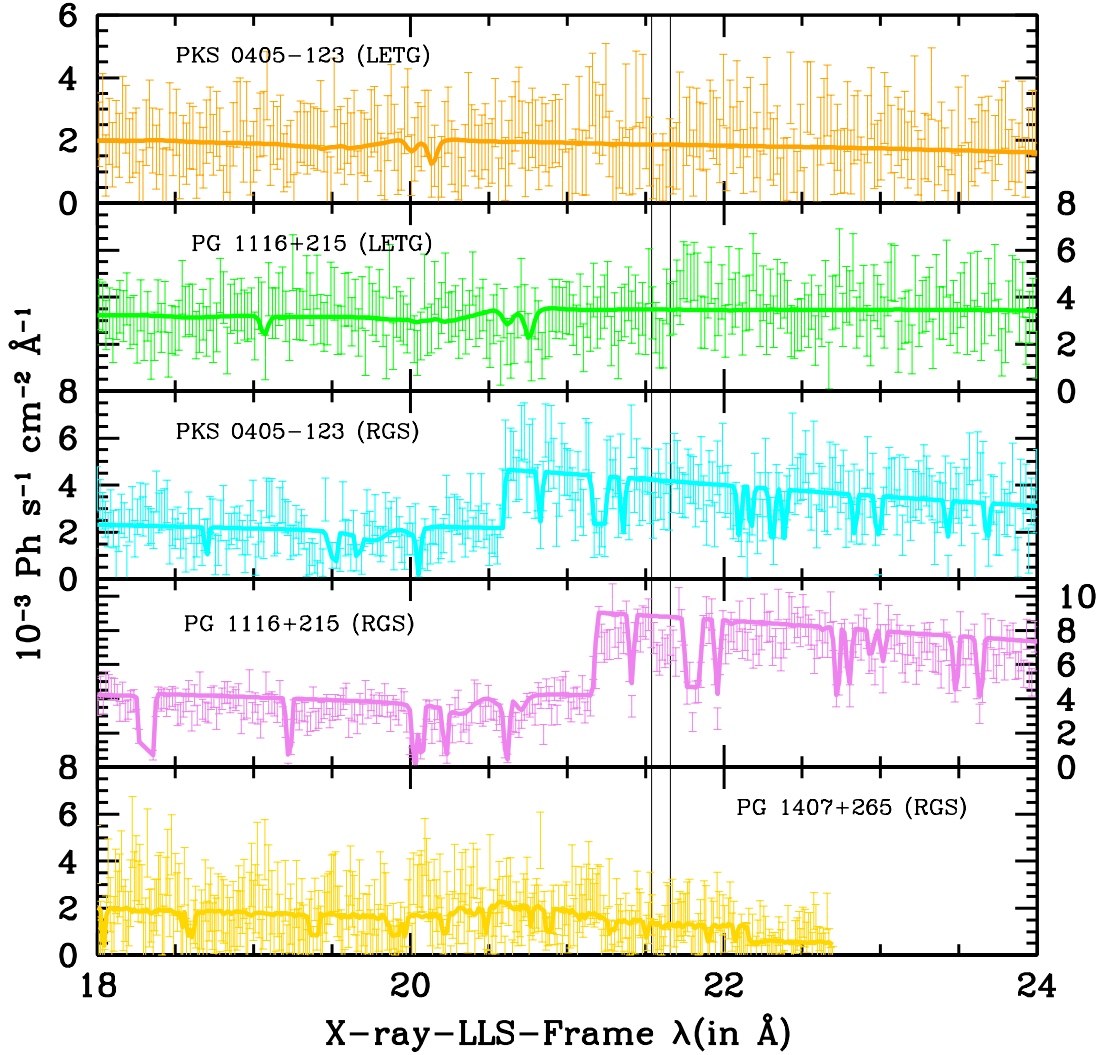


Figure 1. Raw *Chandra* -LETG and *XMM-Newton* -RGS data of the targets of the X-ray halo, in each X-ray-LLS frame 18-24 Å wavelength range (vertical errorbars). In each panel, solid lines are the best-fitting continuum plus Galactic-absorption models. The black rectangle marks the region containing the O VII $K\alpha$ transition.

The lines hinted in the RGS spectrum of PG 1407+265 and in the LETG and RGS spectra of PKS 0405-123 have centroid wavelengths fully consistent with the FUV redshift of their LLSs (vertical red lines in Fig. 7 and 8), while the line seen in the HRC-LETG spectrum of PG 1116+215 is offset by $\sim -1500 \text{ km s}^{-1}$ (130 mÅ at the line wavelength) from the LLS#3 redshift (Fig. 9, red vertical line), and only marginally consistent (at a $\sim 95\%$ confidence level) with it. However such a shift is not seen in the *XMM-Newton* -RGS spectrum of the same target (Fig. 9 in §C), where the O VII $K\alpha$ line is hinted at a redshift consistent with that of LLS#3, and the LETG and RGS line positions are consistent with each other within their 1σ confidence levels (see two purple contours of Fig. 9). This suggests that the displacement of the O VII $K\alpha$ line in the *Chandra* -LETG spectrum of PG 1116+215 is due to either the HRC-LETG wavelength scale uncertainties (see discussion in §C) or the complexity of the procedure of co-adding the 11 observations that make up the total 355 ks *Chandra* -LETG exposure of PG 1116+215 (for comparison, the 375 ks *Chandra* -LETG exposure of PKS 0405-123 is made up of only 4 different observations, and the RGS spectra of PG 1407+265, PKS 0405-123 and PG 1116+215 are made up of only 2, 2 and 6 observations, respectively), or a

combination of both. For this reason, in the following, we use the X-ray-LLS redshifts for all targets, though we also compare the statistical significance of the lines with those derived by using the exact FUV-LLS redshifts.

3.2. Stacked Spectrum of the X-ray Halo

After checking for the presence of O VII $K\alpha$ lines in the single *XMM-Newton* and *Chandra* spectra of our targets, we proceeded to blue-shift the five continuum-normalized spectra to their own X-ray-LLS redshifts, re-grid them over a common 1–35 Å wavelength grid with bin-size of 30 mÅ (about 0.4 and 0.6 times the RGS and LETG LSF-FWHMs, respectively) and stack them together by weighting each spectrum by its relative signal-to-noise ratio per bin (Fig. 2). After each stacking, the normalized spectrum in standard-deviation was checked over its entire band for consistency with Gaussian expectations and, when needed, corrected for the non-Gaussianity introduced by the complexity of the continuum-normalization, de-redshifting, re-gridding and stacking procedures. Practically, after each stacking we computed the fractions $f_p = N_p(\leq 3\sigma)/N_{bin}$ and $f_m = N_m(\leq 3\sigma)/N_{bin}$ of positive and negative 30 mÅ bins not exceeding 3 standard deviations and computed the one-sided Gaussian equivalent number of standard deviations σ_p and σ_m corresponding to the probabilities $(1 - f_p)$ and $(1 - f_m)$. We then multiplied the errors of the > 1 and < 1 bins of the normalized spectrum by the factors $(3/\sigma_p)$ and $(3/\sigma_m)$, respectively, so forcing the data to approach Gaussianity. We note that in all cases, while the probabilities $(1 - f_p)$ were always of the order of $(1 - 0.9973)/2$ (as expected in the Gaussian hypothesis, if no actual physical emission-line is present in the stacked spectra), the probabilities $(1 - f_m)$ were always significantly larger, suggesting that real absorption features are present in the stacked spectra. These should include, not only those associated to the putative hot halo (e.g. O VII, N VI, Ne IX, etc), but also the resonant and photoelectric transitions of, e.g., O I–O III, N I–N III imprinted by the known LLSs along the lines of sight. Indeed, repeating the same calculation by excluding narrow (± 60 mÅ) spectral regions centered on the main hot- and cool-CGM resonant transitions, we find smaller error correction factors, which, in turn, yields to larger line statistical significances in the stacked spectrum. By applying the above correction procedure, and by doing it over the entire unmasked 1–35 Å spectral band, we are therefore conservatively, and artificially, reducing the actual statistical significance of real absorption lines in the spectra (see below).

The procedure described above was used to produce the one-by-one stacking of the five spectra of our three targets shown in the 5 panels of Fig. 2, and it amplifies the real hot-CGM signal, while washing out spurious fluctuations and/or possible quasar or $z = 0$ rest-frame features. Indeed, a strong absorption line-like signal is revealed at the rest-frame wavelengths of the strongest $K\alpha$ and $K\beta$ transitions of the He-like ion of oxygen (Table 4 in §D, bottom panel of Fig. 2 and top panel of Fig. 3). Associated $K\alpha$ and $K\beta$ transitions of He-like nitrogen are also hinted in the stacked spectrum (bottom panel of Fig. 3), albeit at lower statistical significance (Tab. 4 in §D).

3.2.1. Model-Independent Statistical Significance of the X-Ray Halo

After each stacking, we computed model-independent ‘bin-by-bin’ statistical significances of the absorption lines visible in each spectrum. We did this by coadding, in quadrature, the positive and negative (separately) standard deviations of the normalized spectra (corrected for ‘non-Gaussianity’ over the entire spectral band, as described above), in ± 60 mÅ-wide regions (i.e. ± 2 bins, or about $\pm 0.85 \times$ the RGS LSF FWHM) around the rest-frame positions of the four transitions O VII $K\alpha$, O VII $K\beta$ (green shaded rectangles in Fig. 2), N VI $K\alpha$ and N VI $K\beta$, and adopting the net (negative minus positive), standard deviation as statistical significance of the line.

The bin-by-bin statistical significance of the O VII ($K\alpha, K\beta$) and N VI ($K\alpha, K\beta$) transitions at the X-ray-LLS redshifts, are summarized in Table 3, for the continuum-normalized spectra of the single targets, and in the first part Table 4, for the continuum-normalized spectra of the three targets over the stacking procedure (see §D).

The cumulative (i.e. coadded in quadrature) statistical significance of the signal produced by the O VII ($K\alpha + K\beta$) absorbers of our X-ray halo increases monotonically during the stacking procedure, reaching a final value of 5.0σ (top part of Table 4), confirming that the signal is being amplified by the stacking. The associated N VI signal increases also monotonically but only up to the stacking of the *XMM-Newton* -RGS spectrum of PG 1116+215, then it decreases slightly after stacking the last *Chandra* -LETG spectrum of the same target (top part Table 4), again possibly suggesting inaccuracies in the HRC-LETG dispersion relationship (see §C). The final statistical significance of the O VII and N VI transitions in the stacked spectrum of the X-ray halo is 6.2σ . Repeating the above stacking procedure by correcting for non-Gaussianity only over the halo-line-free portions of the data, would yield slightly larger bin-by-bin statistical significances of the O VII ($5.0 \rightarrow 5.2\sigma$) and N VI ($3.7 \rightarrow 3.8\sigma$) lines, taking the cumulative statistical significance of the X-ray halo from 6.2 to 6.4σ . If no error-amplification is applied to the stacked spectrum (i.e. without forcing Gaussianity of the error distribution), the statistical significances of the lines in the final stacked

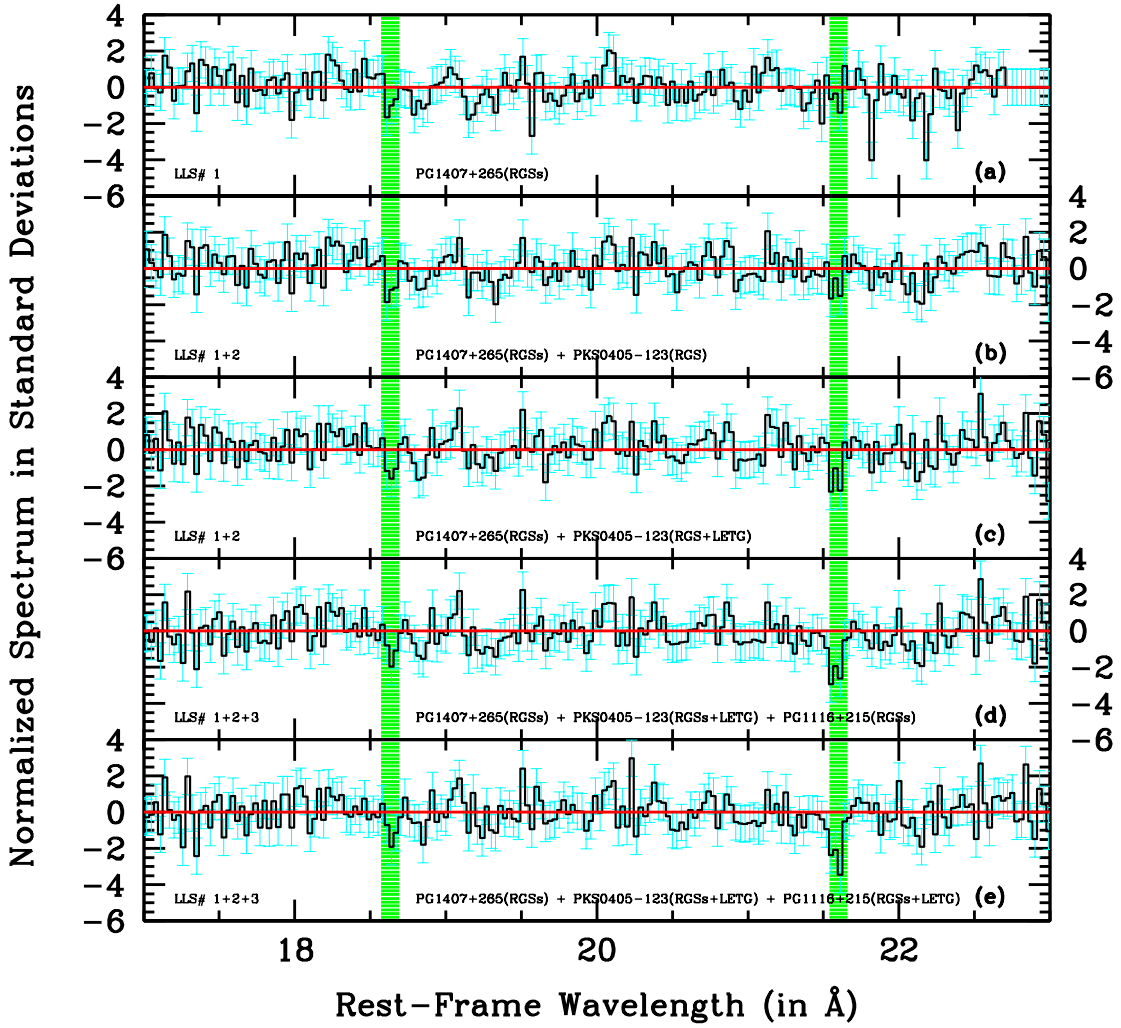


Figure 2. Stacked spectra of the X-ray halo in the X-ray-LLS-frame wavelength scale and in standard deviations. The panels show (in the 17-23 Å wavelength range), respectively: (a) the XMM-RGS spectrum of PG 1407+265 de-redshifted to $z_{X\text{-ray-LLS}\#1}$; (b) the (a)-spectrum coadded to the XMM-RGS spectrum of PKS 0405-123 de-redshifted to $z_{X\text{-ray-LLS}\#2}$; (c) the (b)-spectrum coadded to the *Chandra* -LETG spectrum of PKS 0405-123 de-redshifted to $z_{X\text{-ray-LLS}\#2}$ (d) the (c)-spectrum coadded to the *XMM-Newton* -RGS spectrum of PG 1116+215 de-redshifted to $z_{X\text{-ray-LLS}\#3}$; (e) the (d)-spectrum coadded to the *Chandra*-LETG spectrum of PG 1116+215 de-redshifted to $z_{X\text{-ray-LLS}\#3}$. Error-bars are shown in cyan and represent 1σ errors, after correction for 'non-Gaussianity'. Green shaded areas show the features amplified by the stacking procedure in this wavelength range, namely the O VII $K\alpha$ line at $\lambda = 21.6$ Å and, at lower significances, the O VII $K\beta$ line at $\lambda = 18.63$ Å. Bin-by-bin statistical significances of the hot-CGM lines over the stacking procedure, are listed in Table 4.

spectrum of the X-Ray halo, are 6.9σ , 3.4σ , 4.6σ and 3.2σ , for the O VII $K\alpha$, O VII $K\beta$, N VI $K\alpha$ and N VI $K\beta$, respectively: a final coadded (in quadrature) statistical significance of the X-ray halo of 9.5σ .

Finally, stacking the first four X-ray spectra of Tab. 4 shifted to the exact FUV-LLS redshifts, rather than the best-fitting O VII $K\alpha$ redshifts, does not significantly modify the bin-by-bin statistical significances of the O VII and N VI lines (compare the first four rows of the top and bottom parts of Table 4). It is only after stacking the *Chandra* -LETG spectrum of PG 1116+215, that the bin-by-bin statistical significance of both groups of lines abruptly drops, from $4.8 \rightarrow 4.2\sigma$ (O VII) and $4.3 \rightarrow 3.0\sigma$ (N VI), confirming that these lines are present in the *Chandra* -LETG spectrum of PG 1116+215 at slightly shifted redshifts, compared to the systemic velocity of LLS#3.

3.2.2. Contribution of the O VII and N VI signals to the X-ray halo signal

From Tab. 4, we infer that the quantity $(N_\sigma/\text{SNRE}) \times \Delta\lambda$, a proxy for the line EW , (where $\Delta\lambda$ is the resolution of the spectrometer) roughly halves its value over the stacking, for both the couples of O VII and N VI lines (going from (33 ± 15) mÅ and (21 ± 11) mÅ to (15 ± 3) mÅ and (11 ± 3) mÅ for the O VII and N VI lines, respectively), but is consistent with being constant within the decreasing (with stacking) 1σ uncertainties. This suggests that the amount of hot-CGM probed by our lines of sight (two of which, those with highest SNRE spectra, with very similar galaxy-association parameters: see Table 2) is not widely different in the three halos.

However, while the RGS+LETG spectra of PKS 0405-123 and PG 1116+215 contribute equally to the O VII signal, the N VI signal is dominated by the spectrum of PG 1116+215 (Tab. 3). The combined bin-by-bin statistical significances of the O VII lines are 2.2σ , 3.0σ , and 3.0σ , for PG 1407+265, PKS 0405-123 and PG 1116+215, respectively (Tab. 3), while those of the N VI lines are 2.1σ in the spectrum of PKS 0405-123 (the X-ray spectrum of PG 1417+265 is blind at the LLS-frame wavelength of the N VI $K\alpha$ and $K\beta$ transitions) and 2.7σ in the spectrum of PG 116+215 (Tab. 3). For this reason, we use the bin-by-bin statistical significances of the O VII lines in the spectra of the three targets (σ_{OVI}^i) as weights to compute the average properties of the LLSs and associated galaxies of the X-ray halo (see §B).

3.3. Modeling the X-Ray Halo Spectrum

To confirm the presence of the O VII and N VI absorption lines and evaluate their centroid positions, equivalent widths (EWs, hereinafter) and model-dependent ‘gaussian-fitting’ statistical significances, we modeled the line-like deficits of counts in the stacked normalized spectrum in the X-ray-LLS frame with four unresolved Gaussians folded through an average LETG and RGS Line Spread Function (LSF). We did this by (a) exploiting the ftool (Blackburn 1995) ‘ftfx2xsp’ to convert the blueshifted, regridded and stacked continuum-normalized spectrum (and its ‘super-Poissonian’ errors) of the X-ray halo into a standard PHA format, (b) using the ftool (Blackburn 1995) ‘ftgenrsp’ to build a normalized Photon-Redistribution matrix (RSP) with Gaussians LSF with Full-Width Half Maximum (FWHM) equal to the average RGS and LETG LSF-FWHMs, and (c) fitting the data folded with their response within the fitting-package Sherpa in Ciao (Fruscione et al. 2006).

To model the normalized continuum we used a power-law with spectral index frozen to zero, and normalization free to vary to conservatively allow for an additional correction to a possible residual excess of either negative or positive fluctuations in the stacked broad-band data, compared to the Gaussian hypothesis. For the four absorption lines we used four negative and unresolved (i.e. with FWHM frozen to 50 mÅ, i.e. a value smaller than the instrument LSF FWHM) Gaussians, with line centroid and amplitude (relative to the continuum, i.e. EW) free to vary. The fit yields a continuum fitting normalization $C_n = 0.969 \pm 0.006$ (i.e. departing from unity by 3.1 ± 0.6 %) and the best-fitting line parameters and model-dependent (‘gaussian-fitting’) statistical significances (i.e. the ratio between the line EW and its 1σ error) listed in Table 5 (where we also list the 90% EW upper limit on the undetected H-like oxygen $K\alpha$ transition). Fig. 3 shows the data and best-fitting model (yellow-curve), renormalized to 1 for visualization purposes. Contour plots of the EW-centroid confidence levels of the four absorption lines, are instead shown in Figures 10-13, in §E.

The total (coadded in quadrature) statistical significance of the four lines of the X-ray halo estimated through gaussian-fitting is of 5.3σ (compare with 6.2σ derived by co-adding in quadrature the bin-by-bin residuals of the raw-data). If the spectral fitting is performed on the stacked normalized spectrum in the FUV-LLS (rather than X-ray-LLS) frame, the total statistical significance of the four lines drops to 4.3σ (bottom part of Table 5; compare with bin-by-bin significance of 5.2σ).

4. DISCUSSION

The estimate of the line EWs from highly-ionized oxygen and nitrogen at the redshift of our X-ray halo in its stacked X-ray spectrum, possibly at least partly associated to the moderately-ionized oxygen seen at the LLS redshifts in the FUV spectra of the targets of our sample (Table 2; Fox et al. (2013)), allows us to assess the physical state of the hot-CGM in the X-ray halo.

4.1. Ion Column Densities and Doppler parameter of the Hot-CGM in the X-ray Halo

The resolution of the current X-ray spectrometers is not sufficient to resolve the X-ray-halo lines, thus the estimate of ion column densities N_{ion} and Doppler parameters $b_{ion} = \sqrt{2kT/m_{ion} + \sigma_{turb}^2}$ (where T is the electron temperature

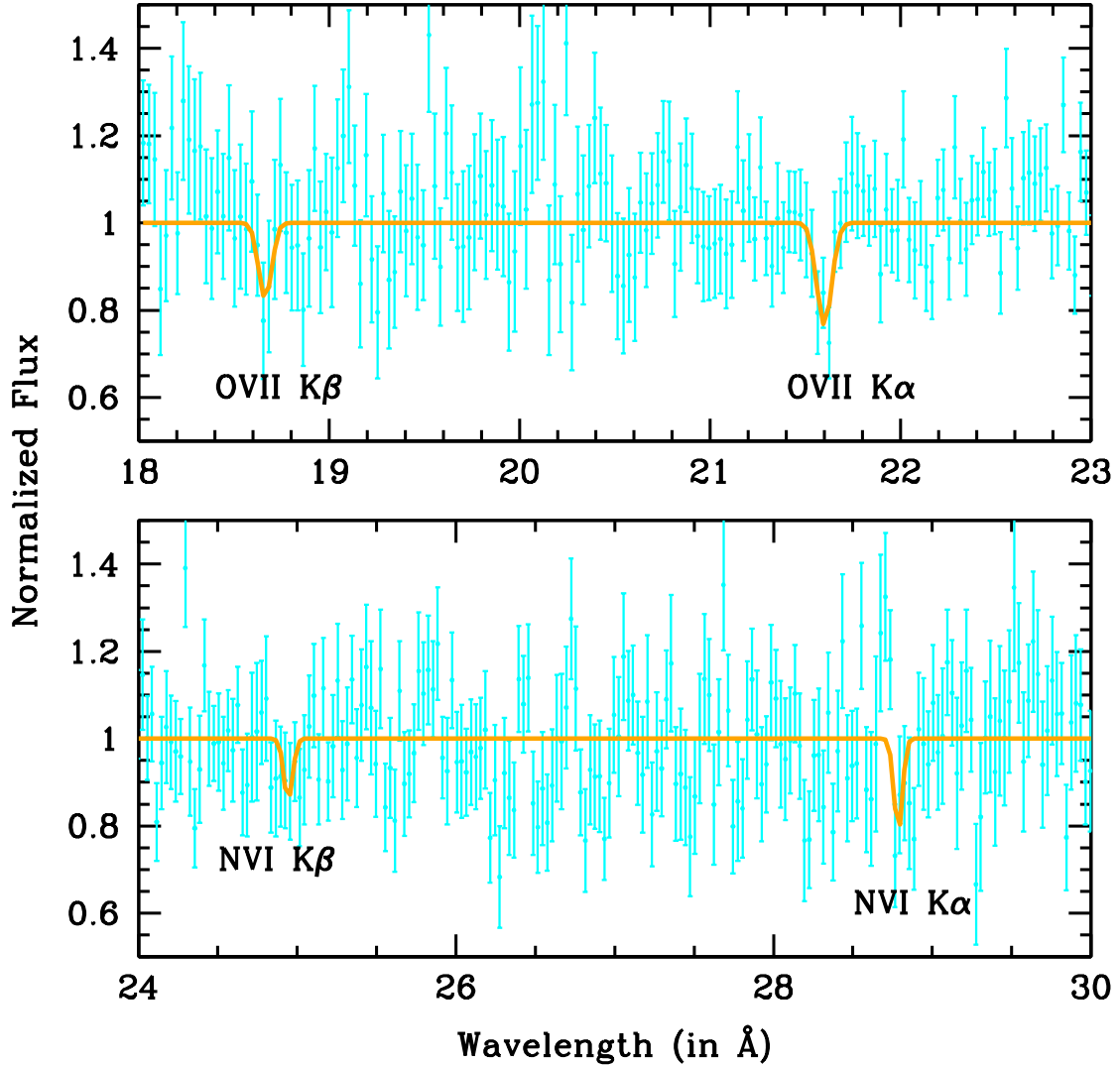


Figure 3. Stacked spectrum of the X-ray halo in actual normalized counts and in the wavelength ranges 18–23 Å (top panel) and 24–30 Å (bottom panel). The spectrum is obtained as described in §3.3, is binned at a resolution of 30 mÅ (about half the LSF-FWHM of both instruments), and has signal-to-noise-per-resolution-element $\text{SNRE}=21.2$ and $\text{SNRE}=19.5$ in the wavelength ranges 18–23 Å and 24–30 Å, respectively. The yellow curve is the best-fitting model, consisting of a constant plus four negative unresolved gaussians with centroid wavelengths and equivalent-widths free to vary in the fit. The fit yields statistical significances of the 4 Gaussians of: 4.2σ (O VII K α), 1.8σ (O VII K β), 2.1σ (N VI K α) and 1.7σ (N VI K β), or a total (in quadrature) statistical significance of 5.3σ , for the hot-CGM in the X-ray halo (Table 5) in §E.

of the gas, m_{ion} the ion mass, k the Boltzmann constant and σ_{turb}^2 the line-of-sight gas turbulence) must rely on the exploitation of curve-of-growth (CoG) techniques. We produced a number of CoGs for each of our four X-ray transition and for ranges of values of $\log N_{ion}$ (in cm^{-2}) = 12–19 and $b_{O,N} = 16 - 300 \text{ km s}^{-1}$ (the low boundary being set by imposing a minimum gas temperature of $T \geq 2.5 \times 10^5 \text{ K}$, needed to start producing sensible fractions ≥ 0.1 of He-like oxygen in CIE gas (see Fig. 14 in §F), and unlikely absence of line-of-sight turbulence motion — $\sigma_{turb}^2 = 0$), and searched for the solutions that matched our EW measurements. These are shown as green and orange shaded regions in Fig. 4, for N_{OVII} and N_{NVI} , respectively. We find the following two broad ion column density intervals $\log N_{OVII}$ (in cm^{-2}) $\simeq 16.3$ –18.6, $\log N_{NVI}$ (in cm^{-2}) $\simeq 15.8$ –17.8 and a common $b_{O,N} \simeq 16$ –170 km s^{-1} .

The range of Doppler parameter values that we measure for oxygen and nitrogen is consistent with many of the LSS O VI Doppler parameters reported in the literature, and in particular with those of our 3 LLSs ($b_{OVI}^i = 28, 78$

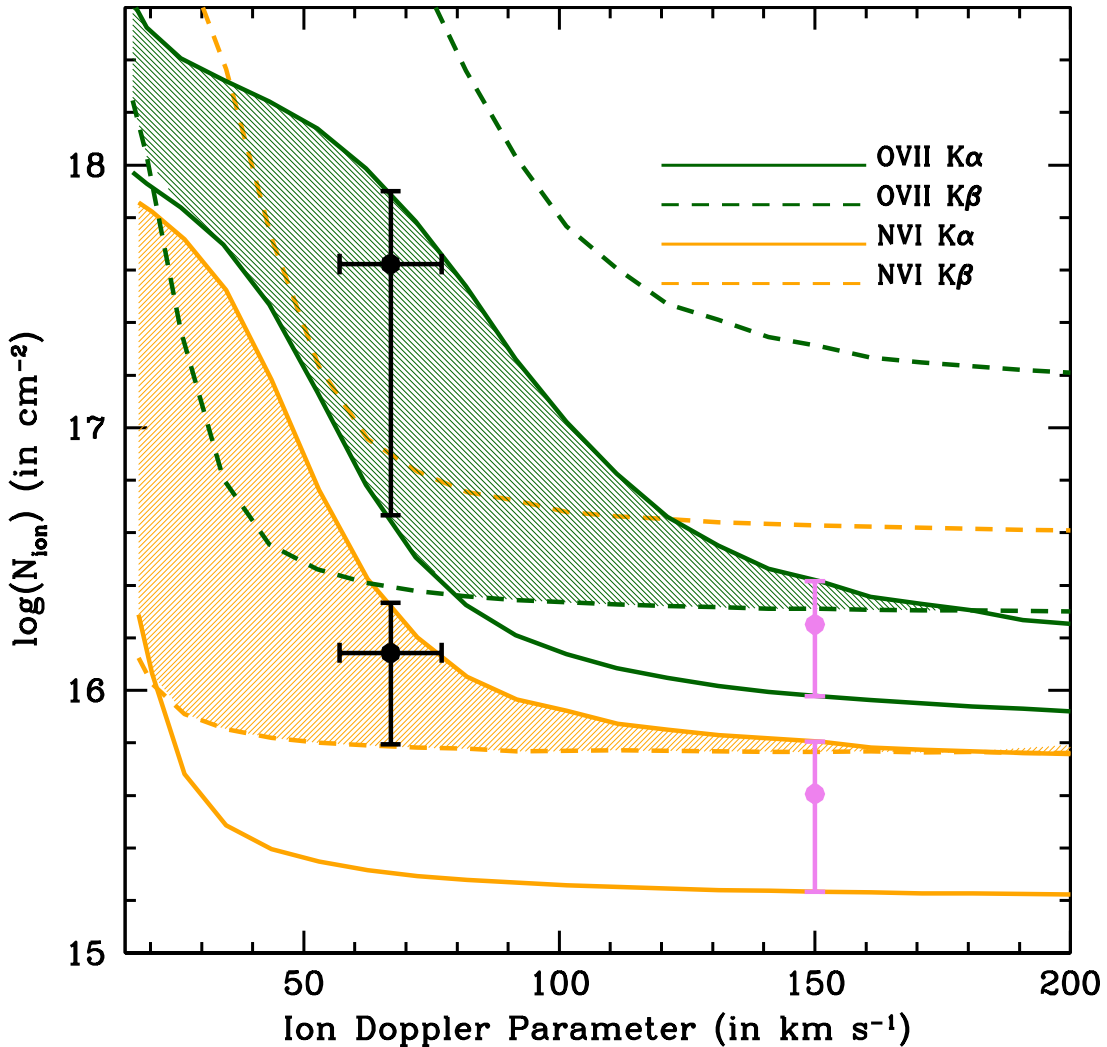


Figure 4. Solid and dashed curves show, respectively, the 1σ $\log N_{\text{ion}}-b$ contours as derived from the $K\alpha$ and $K\beta$ transitions of the X-ray-halo ions O VII (green) and N VI (orange). Shaded green and orange regions show the 1σ $\log N_{\text{O VII}}-b$ and $\log N_{\text{N VI}}-b$ solutions, respectively, while the black points with error-bars mark the solutions at the fiducial $b_{\text{O,N}} = 67 \pm 10$ km s $^{-1}$ value (optically-thick case). Violet points and errorbars, instead, mark the solutions in the optically-thin scenario ($b_{\text{O,N}} = 150$ km s $^{-1}$). For both ions, the 1σ low-boundary constraint on the $K\alpha$ transition (lower solid lines), in either the optically-thick or -thin scenarios, sets a solid floor for the column density of these ions through the X-ray halo, at a distance of 114 kpc from the galaxy’s center.

and 46 km s $^{-1}$, for LLS#1, LLS#2 and LLS#3, respectively; Fox et al. (2013)). If only due to thermal motion (i.e. $\sigma_{\text{turb}}^2 = 0$) this range of $b_{\text{O,N}}$ would correspond to temperatures in the interval $T \simeq (0.25-25) \times 10^6$ K. The exact value of b in this broad interval, however, is not critical with respect to the minimum ion column densities allowed by the X-ray data. Fig. 4, indeed, shows that the $K\beta$ transitions of O VII and N VI (or even just their $K\alpha$ transitions, when considering the $K\beta$ transitions as upper limits and not detections), set stringent lower boundaries to the He-like oxygen and nitrogen column densities (dashed or solid green and orange lower lines, depending on whether $K\beta$ or $K\alpha$ transitions are used, respectively), whose values are virtually independent on the Doppler parameter in the common range $b_{\text{O,N}} \simeq 80-170$ km s $^{-1}$ (i.e. the optically-thin limit for the lines), whereas $16 \lesssim b_{\text{O,N}} \lesssim 80$ km s $^{-1}$ (optically-thick regime) would imply even higher O VII column densities (lower green solid line in Fig. 4). In the following we consider two possible scenarios: (a) the LLS-associated O VI absorbers seen in the FUV spectra of our targets are imprinted at

least partly by the X-ray halo, and (b) the O VI absorbers are not imprinted by the O VII -bearing gas (e.g. [Ahoranta et al. \(2021\)](#)). In both cases, we consider the weighted-average O VI column (plus its 1σ error) as an upper limit for the X-ray halo (see §4.2). In the the first case, we estimate X-ray ion column densities at $b_{O,N} = 67 \pm 10 \text{ km s}^{-1}$, the $(\sigma_{OVII}^i \times N_{OVII}^i)$ -weighted average of the three O VI absorbers (optically-thick case). This corresponds to the X-ray-halo virial temperature $\log T(\text{in K}) \simeq 6$ (see below) for internal line-of-sight turbulence $\sigma_{turb}^2 \simeq 47 - 70 \text{ km s}^{-1}$. In the second scenario, we conservatively assume that the O VII -bearing gas is optically thin, with $b_{O,N} = 150 \text{ km s}^{-1}$ (i.e. dominated by turbulence – $\sigma_{turb}^2 \simeq 147 \text{ km s}^{-1}$ – at the halo virial temperature $\log T(\text{in K}) \simeq 6$) and the lowest possible $N_{OVII,NVI}$ thresholds imposed by their $K\alpha$ transitions.

We find $N_{OVII} = (4.2_{-3.9}^{+7.7}) \times 10^{17} \text{ cm}^{-2}$, $N_{NVI} = (1.4_{-0.8}^{+3.1}) \times 10^{16} \text{ cm}^{-2}$ and $N_{OVIII} \leq 2.9 \times 10^{16} \text{ cm}^{-2}$ (90% confidence), at the common $b_{O,N} = 67 \pm 10 \text{ km s}^{-1}$ (optically thick case (a): black points and error-bars in Fig. 4), or $N_{OVII} = (1.8 \pm 0.8) \times 10^{16} \text{ cm}^{-2}$, $N_{NVI} = (4.0 \pm 2.3) \times 10^{15} \text{ cm}^{-2}$ and $N_{OVIII} \leq 1.3 \times 10^{16} \text{ cm}^{-2}$ (90% confidence), at the common $b_{O,N} = 150 \text{ km s}^{-1}$ (optically thin case (b): violet points and error-bars in Fig. 4).

4.2. Temperature and Equivalent-Hydrogen Column Density

The virial temperature of a $z = 0.295$ halo with $M_h = 10^{12.1} M_\odot$ and $R_{vir} = 200 \text{ kpc}$ (Table 2), is $T_{vir} = \frac{\mu_p G M_h m_p}{2kR_{vir}} \simeq 10^6 \text{ K}$ ([Qu & Bregman 2018](#)), where $\mu_p = 0.59$ is the average weight per particle for a fully ionized gas. At this temperature, He-like and H-like oxygen and nitrogen largely dominate their ionic abundance distribution in CIE gas (left panel of Fig. 14 in §F), with Li-like ions of the same elements being only a small fraction of the total ($\sim 1\%$). Li-like oxygen (and partly also He-like nitrogen), can be more efficiently produced in either CIE gas with $T \lesssim 4 \times 10^5 \text{ K}$ (close to the lowest considered value $T = 2.5 \times 10^5 \text{ K}$ for the O VII -bearing hot-CGM) or in low-density ($n_b < 10^{-4} \text{ cm}^{-3}$) gas photoionized by the external meta-galactic radiation field (left and right panels of Fig.14 in §F). Thus, both the observed O VI and N VI, could at least partly belong to CGM phases different from the O VII -bearing hot-CGM phase, including the possibly photoionized cool-CGM. Moreover, as shown in §3.2.2 the N VI signal is imprinted in the stacked spectrum of the X-ray halo mostly by the LLS#3 galaxy-association, and so may not be fully representative of the average properties of the X-ray halo. In both the optically-thick (case (a)) and optically-thin (case (b)) scenarios, we therefore conservatively infer temperature and hydrogen-equivalent column density of the hot gas permeating the X-ray halo at an average projected distance of 114 kpc from the galaxy center (about $0.6 \times$ the virial radius of our X-ray halo), by combining all the available FUV and X-ray ion column density constraints, but treating the measured N VI (in a solar $[N/O]$ ratio) and average X-ray-halo O VI column densities (plus their 1σ uncertainties) as upper limits (shaded violet and green regions of Fig. 5, respectively).

Practically, we compute ion-by-ion hydrogen-equivalent column densities N_H , by dividing the N_{OVI} , N_{OVII} , N_{OVIII} and N_{NVI} ion column densities by the σ_{OVII}^i -weighted average metallicity $Z = 0.3 Z_\odot$ reported for the three cool LLS absorbers of our sample ([Wotta et al. \(2019\)](#); Table 2) and that we use in a parametric form in the following to explicitly allow for possible hot- and cool-CGM differences, and by the f_{OVI} , f_{OVII} , f_{OVIII} and f_{NVI} ion fractions in CIE gas (see details and caveats in §F) in the temperature range $\log T = 5.4 - 6.6$, and searching for common $\log N_H - T$ solutions. These are shown as orange shaded areas in Fig. 5, left and right panels. In the optically-thick case (Fig. 5, left panel), we find allowed intervals $\log T(\text{in K}) = 5.845 - 6.36$ and $\log N_H(\text{in cm}^{-2}) = (20.02 - 20.59) - \log(Z/0.3Z_\odot)$, while the optically-thin case (Fig. 5, right panel), allows for a wider interval of temperatures $\log T(\text{in K}) = 5.725 - 6.495$, a factor of ~ 3 lower boundary of $\log N_H(\text{in cm}^{-2}) \geq 19.58 - \log(Z/0.3Z_\odot)$, and similar upper boundary $\log N_H(\text{in cm}^{-2}) \geq 20.54 - \log(Z/0.3Z_\odot)$. In both cases, the allowed temperature intervals, encompass the $T_{vir} \simeq 10^6 \text{ K}$ virial temperature of the X-ray halo.

We note that, in either case, by considering N VI as an upper limit (violet shaded area under the violet solid curve of Fig. 5) we are not adding useful constraints to the solution, which is set solely by oxygen ions. In both cases, the allowed interval of temperature is set by the intersections of the X-ray constraints on the O VII column density with the FUV N_{OVI} measurements (considered here as upper limits, green solid curve of Fig. 5) and the X-ray N_{OVIII} upper limit (brown solid curve of Fig. 5), on the lower and upper side, respectively. More importantly, in both cases, the minimum equivalent-hydrogen column density (and so the amount of hot gas in the X-ray halo) is set uniquely by the X-ray constraints on the lowest possible column density of O VII, while its upper boundaries are set again by the FUV N_{OVI} and X-ray N_{OVIII} upper limits, in the optically-thick case, and by the measured X-ray N_{OVII} upper boundary, in the optically-thin case.

Indeed, O VI alone would favor solutions at temperatures $\log T(\text{in K}) \simeq 5.4 - 5.6$ (where the O VI ion fraction is $\gtrsim 0.1$, in CIE gas: see Fig. 14 in §F), which would yield equivalent-hydrogen column densities (and so baryonic mass) at

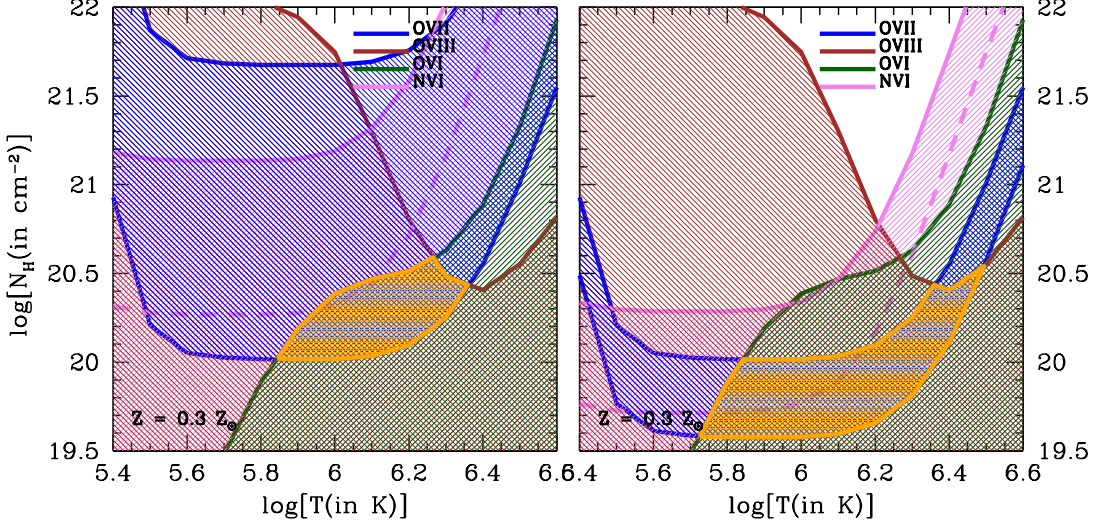


Figure 5. Constraints on the H-equivalent column density of the X-ray halo at a projected distance $\rho = 114$ kpc, obtained by dividing the ion column densities of O VII (blue curves and shaded area), N VI (violet curve and shaded area), O VIII (brown curve and shaded area) and average O VI (green curve and shaded area; Fox et al. (2013)), by their ion fractions in CIE gas (see §F) and by the average $Z = 0.3Z_{\odot}$ metallicity observed for our three cool-CGM systems, as a function of the temperature of the hot-CGM gas. The H-like ion of oxygen is not detected in the X-ray-halo spectrum and its column density curve in the figure is a 90%-confidence upper limit (brown curve and shaded region). N VI and O VI, instead, are detected in the X-ray and FUV spectra, respectively, but are considered here as upper limits to allow for at least a portion of these ions to be produced in physical phases different from the O VII-bearing phase. The left panel is for the optically-thick case, with $b_{O,N} = 67 \pm 10$ km s $^{-1}$ (the weighted-average observed for the O VI absorbers in our LLSs), while the right panel shows solutions for the optically-thin case ($b_{O,N} = 150$ km s $^{-1}$), in which the O VI seen in the FUV are not produced by the O VII-bearing gas.

least an order of magnitude lower than the $\log N_H(\text{in cm}^{-2}) = 20.02 - \log(Z/0.3Z_{\odot})$ boundary set by the O VII X-ray measurements in the optically-thick case, and $> 5\times$ lower than the $\log N_H(\text{in cm}^{-2}) = 19.58 - \log(Z/0.3Z_{\odot})$ boundary set by the O VII X-ray measurements in the optically-thin case.

If only X-ray oxygen data are considered, instead, the low-boundary of the temperature interval is set uniquely by the need of producing detectable fractions of O VII (i.e. $\log T(\text{in K}) \gtrsim 5.4$), but the equivalent-hydrogen column density (and so the baryonic mass: see below) is still lower-bounded at $\log N_H(\text{in cm}^{-2}) \simeq 20.02 - \log(Z/0.3Z_{\odot})$ (optically-thick case) or $\log N_H(\text{in cm}^{-2}) \simeq 19.58 - \log(Z/0.3Z_{\odot})$ (optically-thin case), and allowed to be as large as $\log N_H(\text{in cm}^{-2}) \simeq 20.6 - \log(Z/0.3Z_{\odot})$ (optically-thin case), or implausibly large as $\log N_H(\text{in cm}^{-2}) \simeq 21.6 - \log(Z/0.3Z_{\odot})$ (optically-thick case). It is only by combining the FUV and X-ray column density constraints that we can set stringent lower and upper limits to both the temperature and the equivalent-hydrogen column density (and, in turn, mass: see below) of the X-ray halo. Finally, if we assume that all the observed N VI is produced in the hot-CGM (and thus consider both lower – dashed violet curves – and upper – solid violet curves – boundaries of the measured N VI column density), with Solar [N/O] ratio, the solutions shrink to smaller regions around $\log T(\text{in K}) \simeq 6$, $\log N_H(\text{in cm}^{-2}) \simeq 20.3 - \log(Z/0.3Z_{\odot})$ (optically-thick case) or $\log T(\text{in K}) \simeq 5.76 - 6.16$, $\log N_H(\text{in cm}^{-2}) \simeq (19.72 - 20.06) - \log(Z/0.3Z_{\odot})$ (optically-thin case).

4.3. Mass of the Hot-CGM in the X-ray Halo

In the following we conservatively assume the optically-thin scenario, which provides a solid measurement of the lowest possible equivalent-hydrogen column density of the X-ray halo at a projected distance $\rho = 114$ kpc, to estimate both the line-of-sight volume density of the hot-CGM and its mass.

Our idealized model for the X-ray halo is that of a sphere centered in the galaxy center and filled with 2 gaseous phases (cool and hot, each isothermal) mutually complementing each other spatially. The hot phase is diffuse and extends from the galaxy center out to the virial radius R_{vir} , with density decreasing radially. The cool and condensed phase is that of our three LLSs, observed in the FUV through low-ionization metals and H (e.g. Lehner et al. (2013)).

To estimate the average density of the hot-CGM phase of the X-ray halo, we need to estimate the maximum line-of-sight pathlength available for the hot gas, which, under our assumptions, is simply given by the total available pathlength covered by the X-ray halo at the projected distance ρ minus the thickness of the cool-CGM clouds along the line of sight. With the assumed geometry, the pathlength crossed by our lines of sight at a projected distance ρ and through the X-ray halo, is simply given by $L = 2\sqrt{R_{vir}^2 - \rho^2} \simeq 330$ kpc. The ratio between the total thickness of the cool-CGM clouds along the line of sight (i.e. the diameter of a single spherical cloud times the number of clouds shadowing each other along the line of sight, i.e. [Stocke et al. \(2013\)](#)) and L , defines the line-of-sight covering factor of the cool phase f_l^{cool} . The total thickness of the cool-CGM clouds has been estimated for several LLSs by matching the measured ion column densities with predictions by photoionization-equilibrium models in which a halo cloud of gas with constant density n_H^{cool} is illuminated by the metagalactic radiation field at the redshift of the LLS (e.g. [Lehner et al. \(2013\)](#); [Stocke et al. \(2013\)](#)). For our 3 LLSs [Lehner et al. \(2013\)](#) and [Stocke et al. \(2013\)](#) derive: $N_H = (10^{20}, 10^{18.55}, 10^{19.1}) \text{ cm}^{-2}$ and $n_H = (10^{-3.1}, 10^{-3.1}, 10^{-4}) \text{ cm}^{-3}$ for (LLS#1, LLS#2, LLS#3), respectively. This gives σ_{OVI}^i -weighted averages of $\langle N_H \rangle^{cool} = 10^{19.515} \text{ cm}^{-2}$ and $\langle n_H^{cool} \rangle = 5.4 \times 10^{-4} \text{ cm}^{-3}$ for the cool-CGM of the X-ray halo, and thus a line-of-sight thickness of the clouds of $l(X-ray-halo) \simeq 20$ kpc. This yields a line-of-sight covering factor of the cool-CGM through the X-ray halo $f_l^{cool} = 0.061$.

Finally, the average density of the hot-CGM phase at a projected distance $\rho = 114$ kpc through the X-ray halo, is thus given by $\langle n_H^{hot} \rangle = N_H^{hot} / [(1 - f_l^{cool})L] \simeq (4 - 36) \times 10^{-5} (Z/0.3Z_\odot)^{-1} \text{ cm}^{-3}$, and it modulates by a factor of $n_H^{hot}(@\rho; l=0) / n_H^{hot}(@\rho; l=\pm L/2) \simeq [1 + (L/2\rho)^2]^{3\beta/2} \simeq 3^{3\beta/2}$ from the near-side through the far-side of the halo (here β is the spectral density of the density profile we adopt to estimate the mass of the hot-CGM: see below). The average density is $\lesssim 14(Z/0.3Z_\odot)^{-1} \times$ lower than that estimated for the cool-CGM phase under the pure-photoionization equilibrium and constant gas-density hypothesis. This, combined with temperatures of the two phases that differ by factors ~ 100 , gives pressures that differ by factors $\gtrsim 7(Z/0.3Z_\odot)$. Pressure equilibrium between the two phases would then require either $\gtrsim 7(Z/0.3Z_\odot) \times$ lower temperatures of the hot phase, inconsistent with the reported detection of O VII and N VI species, or $\gtrsim 7(Z/0.3Z_\odot) \times$ lower average densities of the hot-phase along the line of sight, which, in turn, would require unphysically long line-of-sight pathlengths of $\gtrsim 2(Z/0.3Z_\odot)$ Mpc. This suggests that either pressure equilibrium between the two co-existing phases is not at work, or that the cool-CGM clouds are actually $\gtrsim 7(Z/0.3Z_\odot) \times$ denser (and so smaller) than inferred under the pure photo-ionization hypothesis. In the latter case, photo-ionization by the external radiation field would be less effective and alternative (or concurring) ionization mechanisms should be at work (see, e.g. [Bregman et al. \(2018\)](#) and references therein). The cool-CGM clouds would then be pressure-confined by the hot gas (e.g. [Armillotta et al. \(2017\)](#); [Afruni et al. \(2021\)](#) and references therein).

To estimate the mass of the hot phase, we assume a volume filling factor $(1 - f_V^{cool}) = (1 - 0.75 \times f_l^{cool}) \simeq 0.954$, again complementary to that estimated for the cool-CGM (the factor 0.75 accounts for the occurrence of LLS detections in the samples observed with the HST-COS, e.g. [Werk et al. \(2014\)](#) and references therein). For the radial baryon density law of the X-ray halo, we assume a β -profile ([Cavaliere & Fusco-Femiano 1976](#)): $n_H^{hot}(r) = n_0^{hot} [1 + (r/R_c)^2]^{-3\beta/2}$. We integrate the density profile from $r = 0$ up to $r = R_{vir}$ for a number of values of the model parameters, searching for those solutions that match the entire range of allowed hot-CGM N_H observed at the average projected distance of $\rho = 114$ kpc, i.e.:

$$N_H = 2 \int_0^{L/2} n_H^{hot}(r) dl = 2 \int_0^{\alpha_{max}} n_H^{hot}(\alpha; \rho) (\rho / \cos^2 \alpha) d\alpha, \quad (1)$$

where dl is the increment along the line of sight, α is the angle between the projected distance ρ (i.e. the plane of the sky) and the radius of the halo at a line-of-sight depth $l = \sqrt{r^2 - \rho^2} = \rho \tan(\alpha)$, and $\tan(\alpha_{max}) = 2\sqrt{(R_{vir}/\rho)^2 - 1}$.

Our X-ray halo has dynamical mass $M_h \simeq 10^{12.1} M_\odot$, stellar mass $M^* \simeq 10^{10.56} M_\odot$ and, under the pure photoionization equilibrium hypothesis (i.a. assuming an average cloud gas density $\langle n_H \rangle^{cool} = 5.4 \times 10^{-4} \text{ cm}^{-3}$), cool-CGM gas mass $M_{cool-CGM} \simeq 10^{10.42} M_\odot$ (Table 2). This yields a missing baryon mass of $M_{missing} = f_b M_h - M^* - M_{cool-CGM} \simeq 1.35 \times 10^{11} M_\odot$ (where $f_b = 0.157$ is the universal baryon fraction, [Planck Collaboration et al. \(2020\)](#)). By exploring reasonable values of the β -profile parameters, i.e. $n_0^{cool} = 4 \times 10^{-4} - 0.1 \text{ cm}^{-3}$, $R_c = 1 - 5$ kpc (for reference, central volume density and core radius of the hot halo of the Milky-Way have been estimated in the ranges $n_0^{MW} \simeq (0.12 - 1.2) \times 10^{-2} \text{ cm}^{-3}$, $R_c = 1 - 3$, [Bregman et al. \(2018\)](#), or $n_0^{MW} \simeq (0.7 - 6.6) \times 10^{-2} \text{ cm}^{-3}$, $R_c = 0.6 - 2.7$, [Nicastro et al. \(2016b\)](#)) and $\beta = 0.6 - 0.7$ (i.e. centered on the $2/3$ value corresponding to an isothermal halo), and accepting only solutions at radii $r/R_{vir} = 1.000 \pm 0.005$, we find a range of allowed masses $M_{hot-CGM} \simeq (0.6 - 3) \times 10^{11} (Z/0.3Z_\odot)^{-1} M_\odot$, corresponding to temperatures in the interval $\log T(\text{in K}) \simeq 5.73 - 6.4$, for core radii and volume densities in the ranges $R_c = 2 - 5$ kpc, $n_c^{hot} = 0.008 - 0.04 \text{ cm}^{-3}$. This mass is at least as much as the combined mass of the stellar disk

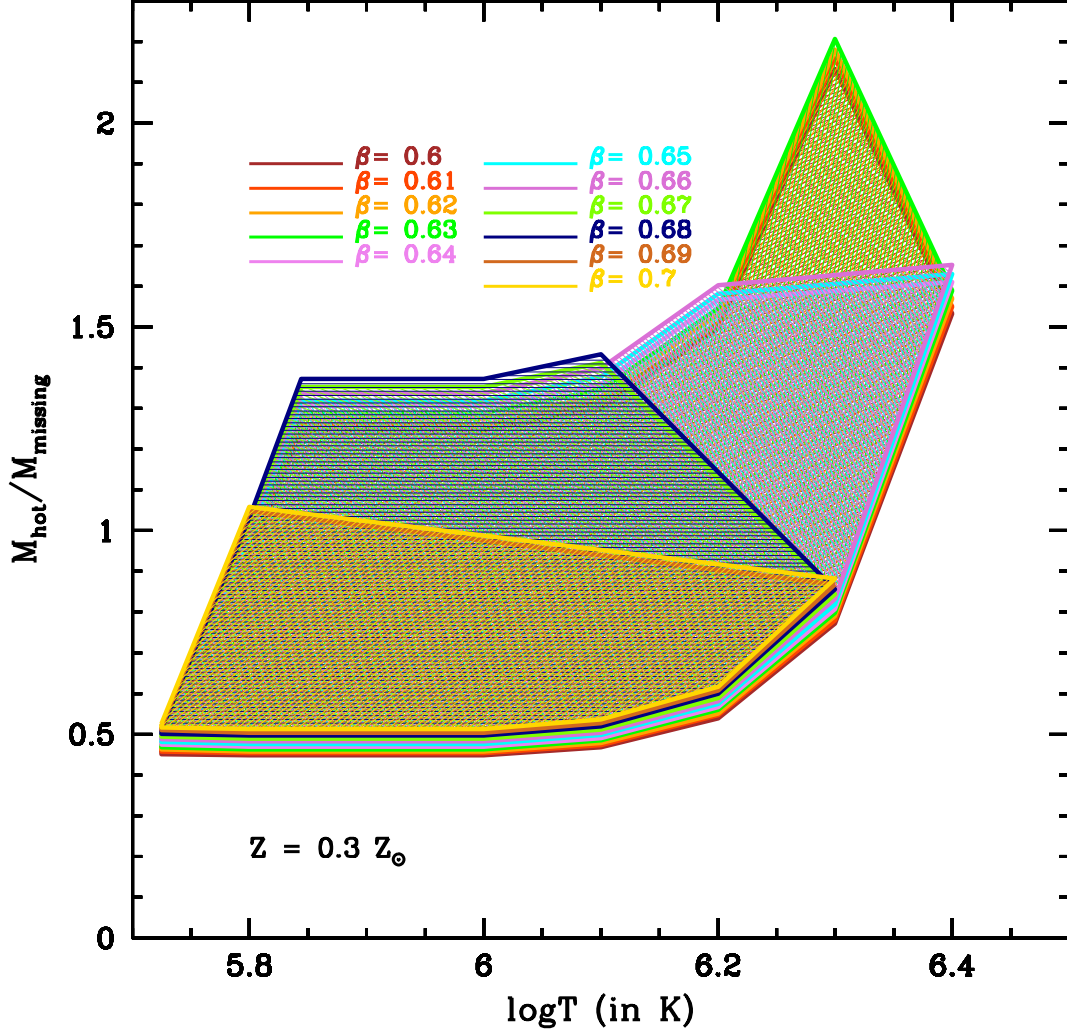


Figure 6. Conservative (i.e. in the optically-thin scenario) constraints on mass and temperature of the hot-CGM in the X-ray halo, for a density spectral index in the range $\beta = 0.6 - 0.7$ (isothermal halo) and hot-CGM metallicity $Z = 0.3Z_{\odot}$. Solutions with $M_{hot-CGM} \simeq M_{missing}$ within R_{vir} , are found in a large interval of temperatures between $\log T(\text{in K}) \simeq 5.8 - 6.35$, for core radii and densities in the ranges $R_c = 1 - 5$ kpc and $n_c^{hot} = 0.008 - 0.04 \text{ cm}^{-3}$, respectively.

and cool-CGM of the X-ray halo and, more importantly, at least half of the galaxy’s missing mass $M_{missing}$. The fraction of hot over missing baryons at the halo virial radius lies in the range $\xi_b = \frac{M_{hot-CGM}}{M_{missing}} \simeq (0.5 - 2.2)(Z/0.3Z_{\odot})^{-1}$, depending on the exact value of the density-profile spectral index β (Fig. 6), with steeper profiles associated to higher central density, and so mass, solutions. At the halo virial temperature the fraction of hot over missing baryons of an isothermal halo ($\beta = 2/3$) lie in the range $\xi_b \simeq (0.5 - 1.4)(Z/0.3Z_{\odot})^{-1}$, with the upper boundary closing the baryon census ($\xi_b = 1$) already at $r \simeq 0.75R_{vir}$.

This not only implies that virtually all the baryons that were still missing can now be accounted for by the hot-CGM gas, but has also important consequences for our understanding of the galaxy-CGM and galaxy-IGM feedback processes throughout the universe lifetime and can help refining feedback prescriptions in hydro-dynamical simulations. A dense hot virialized CGM containing the vast majority of the expected baryons within its virial radius, suggests that accretion mostly occurred in hot-mode and at the rate given by the cosmological baryon fraction (e.g. van de Voort & Schaye (2012)), while the feedback from supernovae and/or past nuclear activity was not sufficiently efficient to expel a significant fraction of the baryons beyond R_{vir} . However, the relative metal richness of the cool- and so probably the hot-CGM (Table 2), may point at an important contribution of feedback (e.g. supernova winds and/or

past nuclear activity) for its metal pollution. In this scenario, we can speculate that the accretion of fresh gas to feed the star formation in the disc likely takes place via a slow cooling of the hot CGM (e.g. Fraternali (2017); Hafen et al. (2022)).

Our simple spherical, isothermal halo filled with a 2-phase (cool and hot) gas, is clearly an idealization. However, the low-boundary mass of the hot component ($M_{hot-CGM} \sim 0.6 \times 10^{11} M_{\odot}$) is a rather strict and conservative limit, imposed solely by the large amount of O VII seen in the stacked X-ray spectrum at a projected distance of $\sim 0.6 R_{vir}$ and in an optically-thin scenario, in which the O VI detected in the FUV is not imprinted by the O VII-bearing gas. Flattening the density profile to $\beta = 0.4 - 0.6$ does not change the minimum fraction of missing mass allowed by the solutions, but slightly lowers its maximum allowed fraction at $\log T(\text{in K}) \lesssim 6.3$ (from $\xi_b \simeq 1.4(Z/0.3Z_{\odot})^{-1}$ to $\simeq 1.2(Z/0.3Z_{\odot})^{-1}$) because of the lower core-density solutions, and can easily accommodate missing-baryon masses well within R_{vir} at $\log T(\text{in K}) \simeq 6.4$, where $\xi_b \simeq 3.8(Z/0.3Z_{\odot})^{-1}$. Reducing the volume covering factor of the hot component, increasing the hot-CGM metallicity to $> 0.3Z_{\odot}$, modifying the geometry of the halo and/or considering non-equilibrium, multi-temperature, collisional-ionization models (e.g. Gnat & Sternberg (2007)), can help reducing the mass of the O VII-bearing gas but would still leave large portions of the density-profile parameter space for solutions that close the galaxy baryon census.

5. CONCLUSIONS

We reported the first direct detection of O VII, and possibly N VI, absorption in the stacked X-ray spectra of three LLSs+O VI absorbers seen in the FUV and associated to the halos of three $\sim L^*$ galaxies. We identify the X-ray absorbers with large amounts of hot gas co-existing with the cool-CGM of these systems and filling their halos. In summary, we found that:

- the X-ray halo is detected in the stacked X-ray spectra of the three quasars PG 1417+265, PKS 0405-123 and PG 1116+215 at conservative statistical significances of 4.6σ (O VII) and 2.7σ (N VI), a combined (in quadrature) statistical significance of 5.3σ ;
- the properties of the X-ray halo are those of the halo of a $\sim L^*$ galaxy, with virial radius $R_{vir} \simeq 200$ kpc, virial temperature $T_{vir} \simeq 10^6$ K, and mass $M_h = 10^{12.1} M_{\odot}$;
- we estimate the mass of the cool-CGM phase of the X-ray halo to be of the order of the average stellar mass of the three galaxies that host it, i.e. $M_{cool-CGM} = 10^{10.42} M_{\odot}$, which leaves a missing baryon mass in the system $M_{missing} \simeq 1.35 \times 10^{11} M_{\odot}$;
- our line of sight intercepts the X-ray halo at weighted-average projected distance of $\rho = 114$ kpc, i.e. $\simeq 0.6 R_{vir}$ and, in a spherical configuration, has a pathlength of $L = 330$ kpc through the halo, along which we estimate equivalent-hydrogen column densities of the O VII-bearing gas $\log N_H(\text{in cm}^{-2}) = (20.02-20.59)(Z/0.3Z_{\odot})^{-1}$, at $b_{O,N} = 62 \pm 10 \text{ km s}^{-1}$ (optically-thick scenario) or, more conservatively, $\log N_H(\text{in cm}^{-2}) = (19.58-20.54) - \log(Z/0.3Z_{\odot})$, at $b_{O,N} = 150 \text{ km s}^{-1}$ (optically-thin case);
- by assuming a spherical geometry and a β density-profile for the X-ray halo, we derive hot-CGM masses in the range $M_{hot-CGM} = (0.6-3) \times 10^{11} (Z/0.3Z_{\odot})^{-1} M_{\odot}$, corresponding to missing-baryon fractions $\xi_b = \frac{M_{hot-CGM}}{M_{missing}} = (0.5-2.2)(Z/0.3Z_{\odot})^{-1}$, and temperatures in the interval $\log T(\text{in K}) \simeq 5.73-6.4$, which comprises the X-ray-halo virial temperature $T_{vir} \simeq 10^6$ K.

Our findings imply that virtually all the baryons that were still missing in typical L^* galaxies, can now be accounted for by the hot-CGM gas. This has important consequences for our understanding of the galaxy-CGM and galaxy-IGM feedback processes throughout the universe lifetime, suggesting that accretion in these galaxies mostly occurred in hot-mode and at the rate given by the cosmological baryon fraction. Feedback from internal activity was efficient in metal-polluting the CGM and perhaps hampering its cooling, but not sufficient to expel a significative fraction of the baryons beyond R_{vir} .

Table 1. *Properties of the X-ray Spectra of the X-ray-Halo Sample*

QSO	LLS	z_{em}	Exposure (ks)		a SNRE	
			RGS1+RGS2	LETG	RGS1+RGS2	LETG
PG 1407+265	1	0.94	213	NA	4.6	NA
PKS 0405-123	2	0.5726	338	376	7.7	5.7
PG 1116+215	3	0.1756	776	355	14	11
Stacked X-ray-halo Spectrum						
Tot & Averages	NA	NA	1327	731	16.6	12.4

^a Signal-to-Noise per Resolution Element in the LLS-frame 18–22 Å spectral range, where the O VII K_α and K_β transitions lie.

We thank an anonymous referee for the useful comments and suggestions, which significantly helped improving the paper. F.N., S.B., M.B, A.B., A.D.R., C.F., E.P. and L.Z. acknowledge support from INAF-PRIN grant “A Systematic Study of the largest reservoir of baryons and metals in the universe: the circum-galactic medium of galaxies” (#1.05.01.85.10). T.F. acknowledges support by the National Key R&D Program of China No. 2017YFA0402600, NSFC grants No. 11890692 and 12133008 and the science research grants from the China Manned Space Project with NO. CMS-CSST-2021-A04.

Facilities: *XMM-Newton* (RGS), *Chandra* (LETG), HST(COS)

APPENDIX

A. SELECTION OF THE X-RAY-HALO SAMPLE

We cross-correlated the *XMM-Newton* RGS and *Chandra* High Resolution Camera (HRC, Murray et al. (2000)) LETG archives with the LLS samples of Lehner et al. (2013) and Prochaska et al. (2019), consisting of 30 quasars observed with the HST-COS crossing LLSs with moderate HI column density ($16.2 \leq \log N_{HI}(\text{in cm}^{-2}) \leq 19$) and associated low- and moderate-ionization metal absorbers (Fox et al. 2013; Lehner et al. 2013). We found 11 matches. Seven of these have more than one *XMM-Newton* RGS public observations, while the remaining four objects have been observed only once and with very short exposures (16-28 ks each) and were removed from the sample. Of the 7 targets with multiple RGS spectra, one is a calibration source and was observed several arcminutes off the aimpoint, thus with a severely degraded spectral resolution. This source was also removed from the sample. We downloaded all the available RGS data of the remaining 6 targets and reprocessed them with the latest version of the *XMM-Newton* Science Analysis Software (SAS v. 20.0.0) and calibration, to produce a final co-added RGS1+RGS2 spectrum of each target.

Two of the six objects of our *XMM-Newton* sample have also multiple *Chandra* HRC-LETG observations publicly available. We downloaded these *Chandra* observations and reprocessed them with the latest version of the *Chandra* Interactive Software of Observations (CIAO v.4.14), Fruscione et al. (2006), to produce final total LETG spectra of these targets.

Finally, we imposed the two following selection criteria to the targets of our sample: (a) that their total RGS and LETG spectra have signal-to-noise per resolution element $\text{SNRE} \geq 4$ in the continuum adjacent the LLS-frame O VII K_α transition (i.e. ≥ 16 net counts per resolution elements, to guarantee the use of Poissonian statistics on the data) and (b) that the LLSs detected along their lines of sight have been confidently associated to Milky-Way-like galaxies, down to sub- L^* luminosities (e.g. Lehner et al. (2013)). This reduced the final X-ray-halo sample to 3 targets, with a total of 5 X-ray spectra: 3 *XMM-Newton* -RGS and 2 *Chandra* -LETG.

Table 1 summarizes the properties of the targets of our X-ray-halo sample and their X-ray spectra. The last row of Table 1 lists the total available X-ray exposure and SNREs (added in quadrature).

Table 2. *Properties of the LSS and the X-ray Halo*

QSO (LLS #)	z_{LLS}	M_* (in $\log M_\odot$)	M_h (in $\log M_\odot$)	R_{vir} (in kpc)	ρ (in kpc)	[X/H]	$\log N_{HI}$ (in cm^{-2})	$\log N_{OVI}$ (in cm^{-2})
PG 1407+265 (#1)	0.6828	^a 10.9	12.4	^a 220	^a 91	^b -1.66	^b 16.41 ± 0.01	^c 13.99 ± 0.06
PKS 0405-123 (#2)	0.1672	^d 10.3	^d 11.9	^d 183	^d 117	^b -0.29	^b 16.45 ± 0.05	^c 14.59 ± 0.05
PG 1116+215 (#3)	0.1385	^e 10.3	11.9	^f 192	^g 127	^b -0.56	^b 16.22 ± 0.02	^c 13.85 ± 0.05
X-ray Halo								
Weighted Averages	0.295	10.56	12.1	200	114	-0.52	16.37 ± 0.03	14.29 ± 0.05

^aBurchett et al. (2019). ^bWotta et al. (2019). ^cFox et al. (2013). ^dBerg et al. (2023). ^eAssumed to be the same as PKS 0405-123, given the same halo mass. ^fKeeney et al. (2017). ^gLehner et al. (2013).

B. PROPERTIES OF THE LLS AND THE X-RAY HALO

Table 2 lists the properties of the LLS–galaxy associations relevant to this work: namely the stellar-mass M_* , halo mass M_h (defined as M_{200} ²) and virial radius $R_{vir} = R_{200}$ of the galaxies, together with the metallicity of the cool-CGM in the LLSs and the impact parameter ρ .

Virial radii of the galaxy-associations are reported in the literature for all three LLSs of our X-ray halo (Berg et al. 2023; Keeney et al. 2017; Burchett et al. 2019), while the halo mass is reported only for the LSS#2 along the sightline to PKS 0405-123 (Berg et al. 2023). For LLS#2 Berg and collaborators (2023) estimate M_h via the stellar-mass–halo-mass relation, as in Rodríguez-Puebla et al. (2017), and then derive R_{vir} via the relationship $M_h = 4/3\pi R_{vir}^3 \Delta_{200} \rho_c(z)$, where $\rho_c(z) = (3H_0^2/8\pi G)[\Omega_m(1+z)^3 + \Omega_\Lambda]$ is the critical density of the universe at redshift z . For the other two LSSs R_{vir} is derived in Keeney et al. (2017) and Burchett et al. (2019) through abundance-matching, i.e. via the galaxy’s optical luminosity, by matching an observed galaxy luminosity function with a theoretical halo-mass function. For these two galaxy-associations, we derive M_h from R_{vir} , again as in Berg et al. (2023), through the relationship $M_h = 4/3\pi R_{vir}^3 \Delta_{200} \rho_c(z)$. Finally, the last row of Table 2 lists the property of the X-ray halo that we use in this work. These are derived by weighting the quantities in rows 1–3 by the statistical significance of the O VII lines ($K\alpha+K\beta$) in the spectra of our three targets (i.e. $\sigma_{OVI}^i = 2.2, 3.0$ and 3.0 for PG 1407+265, PKS 0405-123 and PG 1116+215, respectively: Tab. 3), and averaging them.

C. UNCERTAINTIES IN THE HRC-LETG WAVELENGTH SCALE.

Figures 7–9 show the confidence-level contours of the O VII $K\alpha$ line flux and centroid hinted in the *XMM-Newton* -RGS and *Chandra* -LETG spectra of our three targets. For all spectra, except the *Chandra* HRC-LETG spectrum of PG 1116+215 (made up of 11 different observations), the line centroid is consistent (within $\sim 1\sigma$) with the expected position of the O VII $K\alpha$ transitions at the FUV-LLS redshifts (vertical red lines in Fig. 7–9).

The displacement of the line position in the *Chandra* spectrum of PG 1116+215, could at least partly be due to the large systematic uncertainties that affect the HRC-LETG dispersion relationship. The wavelength scale of the HRC-LETG spectrometer suffers uncertainties of up to 50 mÅ (about 600 km s⁻¹ at the line wavelength), due to the non-linearity of the dispersion relationship, which, in turn, is due to the non-linear imaging distortions of the HRC-S detector³. Such distortions are randomly spaced in wavelengths across the entire spectrum and therefore cannot be calibrated based on the presence of strong lines with known positions in different regions of the same spectrum (which, in any case, are not present in the LETG spectrum of PG 1116+215). Moreover, the 50 mÅ calibration uncertainty quoted above has been derived for the strong FeXVII ($\lambda \simeq 15$ Å) emission line of a very bright X-ray star (Capella). The uncertainty in the aspect reconstruction of the dispersion-relation may be larger for fainter lines, especially in absorption against relatively low-flux continua, and would propagate randomly when adding together different observations of the same source.

Finally, it is also possible that the X-ray lines hinted in the RGS and LETG spectra of PG 1116+215 are probing hot-CGM gas at a velocity slightly offset compared to that of the cool-CGM, though, in that case, the OVI absorber reported by Fox et al. (2013) would not be directly associated with the X-ray system.

² the mass embedded in a sphere with radius R_{200}

³ <https://cxc.cfa.harvard.edu/cal/letg/Corrlam/>

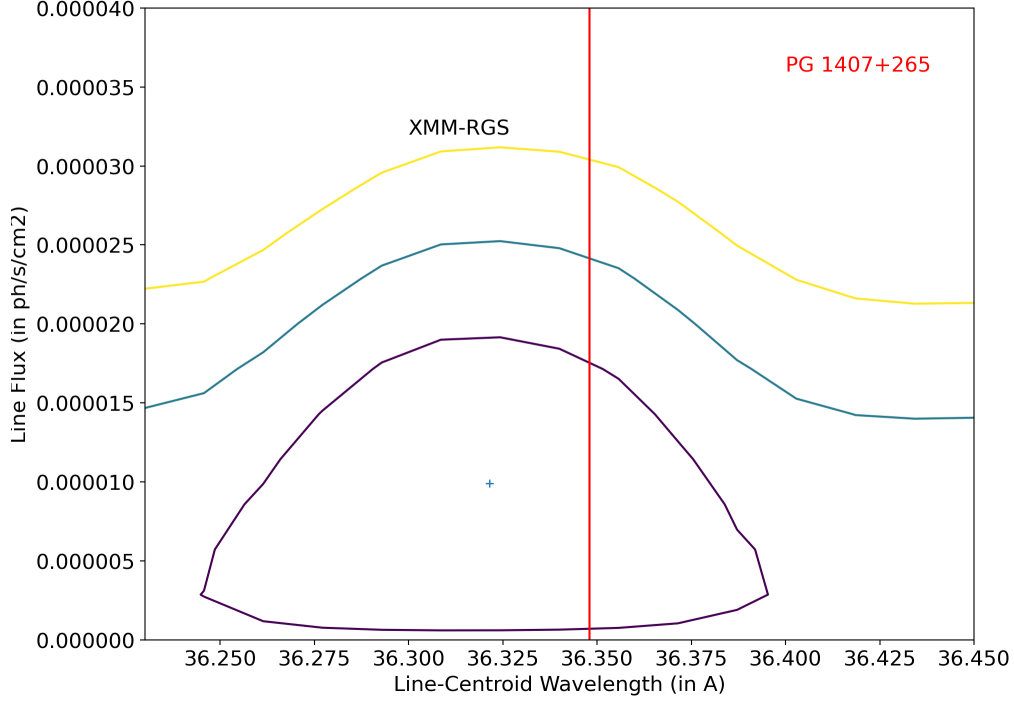


Figure 7. Purple, cyan and yellow curves, are the 68%, 95% and 99.7% confidence level contours (for two interesting parameters) of the line flux and centroid wavelength. The line is hinted at a significance level of only 1σ , at a redshift consistent with that of the LLS#1 absorber (vertical red line).

D. BIN-BY-BIN STATISTICAL SIGNIFICANCES OF THE X-RAY LINES

Table 3 lists the bin-by-bin statistical significances of the X-ray halo lines in the continuum-normalized spectra of our three targets, namely: the *XMM-Newton* -RGS spectrum of PG 1407+265 and the combined *XMM-Newton* -RGS+*Chandra* -LETG spectra of PKS 0405-123 and PG 1116+215.

Table 3. Bin-by-bin statistical significance of the X-ray-halo lines in the single spectra of the three targets

X-Ray Spectrum	$\sigma(\text{O vii})$	$\sigma(\text{O vii})$	$\sigma(\text{O vii})$	$\sigma(\text{N vi})$	$\sigma(\text{N vi})$	$\sigma(\text{N vi})$	σ_{Tot}
	K α	K β	K α + K β	K α	K β	K α + K β	
PG 1407+265 RGS	1.1	1.9	2.2	NA	NA	NA	2.2
PKS 0405-123 LETG	2.7	1.3	3.0	1.9	0.9	2.1	3.7
PG 1116+215 RGS	2.8	1.1	3.0	2.1	1.7	2.7	4.0

Table 4 lists the bin-by-bin statistical significances of the X-ray halo lines derived over the stacking procedure of the continuum-normalized spectra of our three targets, at the X-Ray-LLS redshifts (top part of the table) and the FUV-LLS redshifts (bottom part of the table).

E. SPECTRAL FITTING

Table 5 lists the O VII and N VI best-fitting X-ray halo line parameters and statistical significances (evaluated as ratio between the best-fitting Gaussian line EW and its 1σ error). The top part of the Table is the result of the fit to the stacked spectrum built by shifting the individual spectra to their X-ray-LLS redshifts, while the bottom part lists the best-fitting parameters obtained on the spectrum built by shifting the individual spectra to their FUV-LLS redshifts.

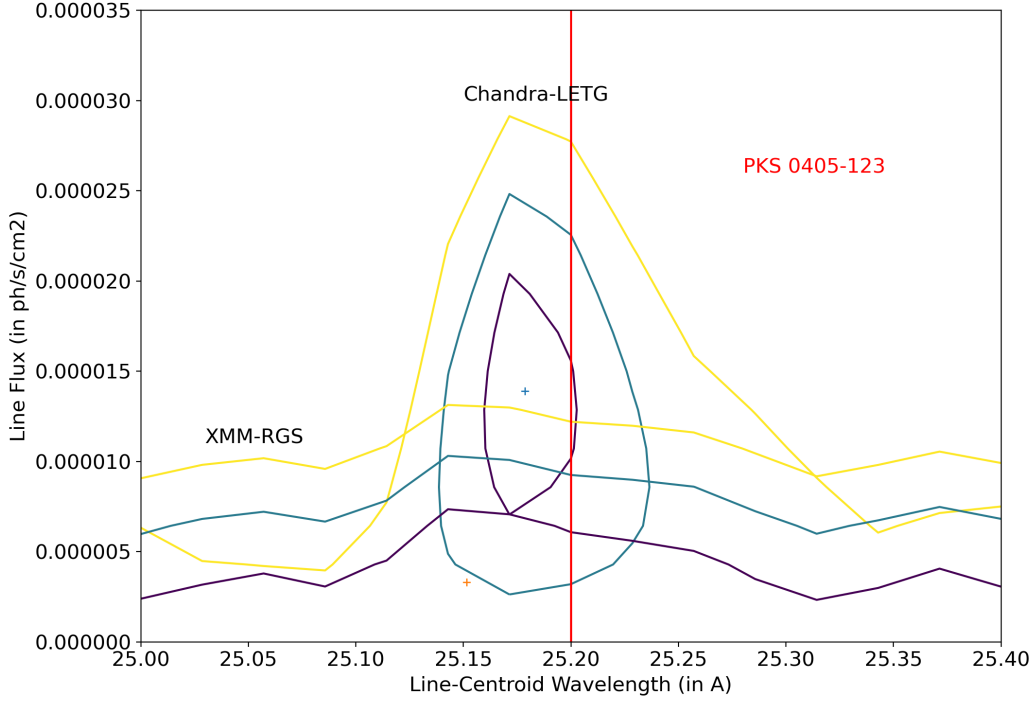


Figure 8. Same as Fig. 7, for the X-ray spectra of PKS 0405-123. The line is hinted at a significance level of slightly more than 2σ in the LETG spectrum, at a redshift consistent with that of the LLS#2 absorber (vertical red line; Mathur et al. (2021)). The best-fitting line-centroid wavelength in the RGS spectrum (red cross) is less than one resolution element from both the line-centroid wavelength of the LETG spectrum and the redshift of the LLS#2 absorber, but the line is only marginally seen in this spectrum (at these wavelengths LETG and RGS spectra have similar SNRE, but the LETG has a $1.5\times$ better spectral resolution than the RGS: compare, e.g., the widths of the 1σ contours of LETG and RGS in Fig. 9).

Table 4. Bin-by-bin statistical Significance of the X-ray-halo lines over the Stacking

X-Ray Spectrum	SNRE 18-22 Å	$\sigma(\text{O vii})$ K α	$\sigma(\text{O vii})$ K β	$\sigma(\text{O vii})$ K α + K β	SNRE 24-28 Å	$\sigma(\text{N vi})$ K α	$\sigma(\text{N vi})$ K β	$\sigma(\text{N vi})$ K α + K β	σ_{Tot}
X-ray Redshifts									
PG 1407+265 RGS	4.6	1.1	1.9	2.2	NA	NA	NA	NA	2.2
+ PKS 0405-123 RGS	9.0	2.2	2.3	3.2	6.3	1.6	1.1	1.9	3.7
+ PKS 0405-123 LETG	10.7	3.4	2.1	4.0	7.7	1.9	0.9	2.1	4.5
+ PG 1116+215 RGS	17.6	4.3	2.2	4.8	16.2	3.2	2.4	4.0	6.2
+ PG 1116+215 LETG	20.8	4.5	2.2	5.0	19.4	3.0	2.1	3.7	6.2
LLS's Redshifts									
PG 1407+265 RGS	4.6	1.1	1.9	2.2	NA	NA	NA	NA	2.2
+ PKS 0405-123 RGS	9.0	2.2	2.3	3.2	6.3	1.6	1.1	1.9	3.7
+ PKS 0405-123 LETG	10.7	3.3	2.2	4.0	7.7	1.9	1.2	2.2	4.6
+ PG 1116+215 RGS	17.6	4.2	2.4	4.8	16.2	3.4	2.7	4.3	6.4
+ PG 1116+215 LETG	20.8	3.4	2.4	4.2	19.4	1.4	2.7	3.0	5.2

Contour plots of the EW-centroid confidence levels of the four absorption lines, are shown in Figures 10-13.

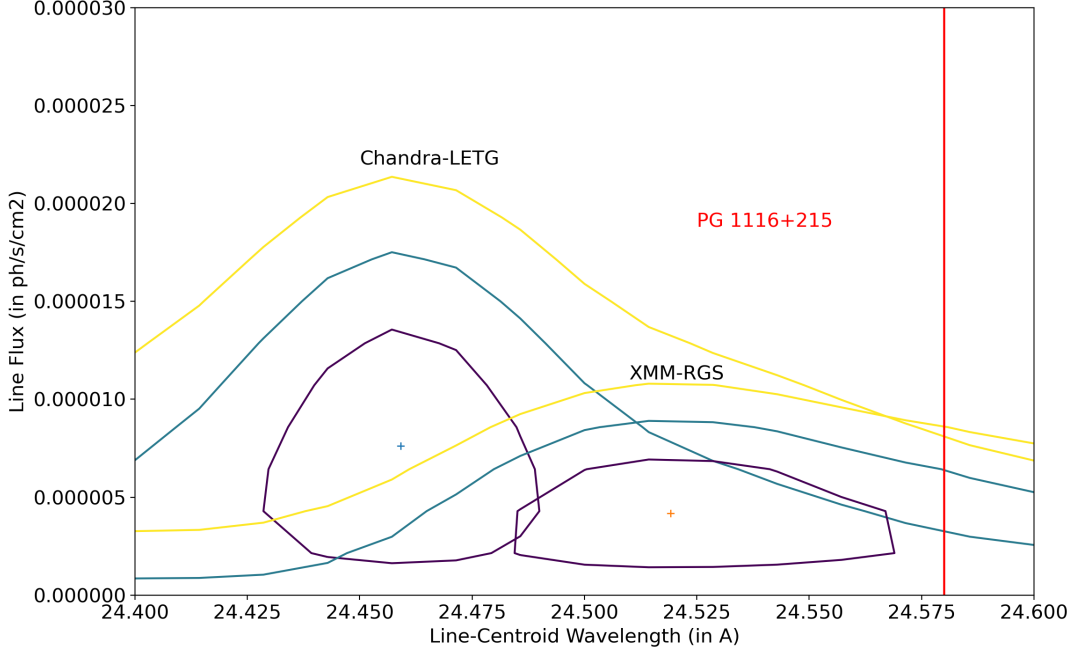


Figure 9. Same as Fig. 7, for the X-ray spectra of PG 1116+215. The line is hinted at a significance level slightly above 1σ in both spectra, and at consistent fluxes. However, only the redshift of the line of the RGS spectrum is consistent (within $\sim 1\sigma$) with the redshift of the LLS#3 absorber (vertical red line). The position of the line in the HRC-LETG spectrum (which suffers non-linearity effects that affect the aspect-reconstruction of the dispersion-relation), is only marginally (at $2-3\sigma$ level) consistent with the redshift of the LLS#3 absorber.

Table 5. *Best-fitting hot-CGM absorption line parameters*

Line Parameter	O VII K α	O VII K β	N VI K α	N VI K β	O VIII K α
X-Ray Redshifts					
Centroid (in Å)	21.60 ± 0.03	$18.66^{+0.03}_{-0.02}$	$28.79^{+0.10}_{-0.02}$	24.94 ± 0.09	^a 18.97
EW (in mÅ)	23.0 ± 5.5	$15.0^{+8.5}_{-8.3}$	14.3 ± 6.8	9.9 ± 6.0	≤ 12.0
Significance	4.2σ	1.8σ	2.1σ	1.7σ	90%
LLS's Redshifts					
Centroid (in Å)	21.57 ± 0.02	18.66 ± 0.02	$28.9^{+1.8}_{-0.9}$	24.93 ± 0.02	^a 18.97
EW (in mÅ)	16.1 ± 6.2	14.9 ± 8.7	14.4 ± 6.7	13.0 ± 6.2	≤ 12.0
Significance	2.6σ	1.7σ	2.1σ	2.1σ	90%

^a Frozen in the fit.

F. ION FRACTIONS IN CIE AND PIE GAS

Figure 14 shows the fractional abundances of the ions O VI (green), O VII (blue), O VIII (brown) and N VI (violet) as a function of temperature (left panel) and hydrogen density (right panel), in gas in collisional ionization equilibrium (CIE; left panel) and photoionized by the average meta-galactic radiation field at the redshift of the X-ray halo (PIE, Nicastro et al. (2016a); right panel), respectively.

In CIE gas (left panel) O VII and N VI are effectively the only populated ions of oxygen and nitrogen at $\log T(\text{in K}) \simeq 5.7 - 6.0$ (the virial temperature range for halo masses in the range of $M_h \simeq 10^{11.8-12.1} M_\odot$, at the X-ray halo redshift $z = 0.295$), while O VI and O VIII fractions peak, respectively, at the opposite extremes of the considered

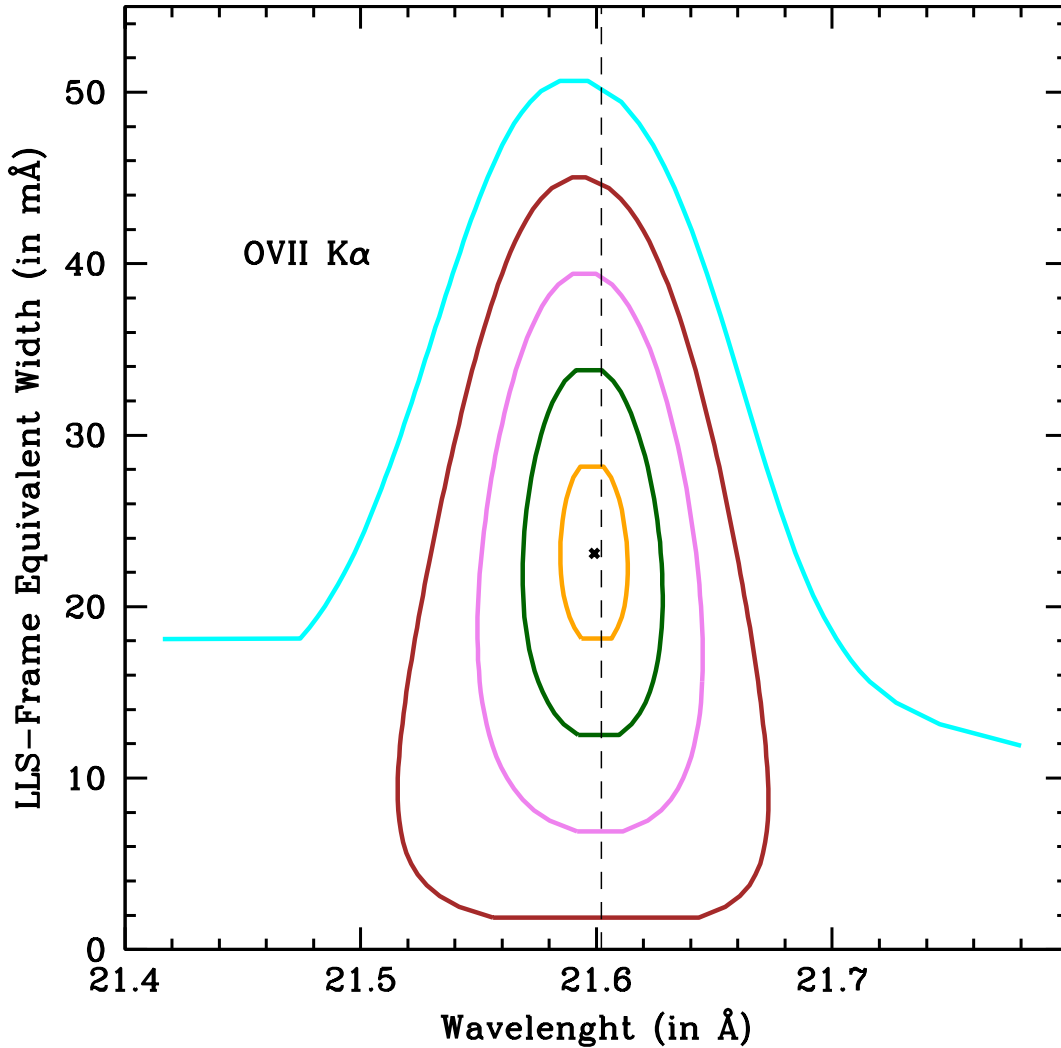


Figure 10. Orange, green, violet, brown and cyan curves show the 1σ , 2σ , 3σ , 4σ and 5σ confidence levels (for one interesting parameter) in the line EW–centroid space, for the O VII $K\alpha$ transition imprinted by the hot-CGM of our X-ray halo. The black cross shows the best-fitting line parameters in the LLS-frame. The best-fitting line-centroid is virtually coincident with the rest-frame wavelength of the transition (dashed vertical line).

temperature range, namely $\log T(\text{in K}) \simeq 5.45$ and $T(\text{in K}) \simeq 6.4$, and reach maximum abundances of only 20 and 40%. Moreover, at the O VI peak temperature, the He-like ions of nitrogen is still largely populated, while the corresponding oxygen ion has a fraction of only $\sim 20\%$, and so difficult to detect in current moderate-resolution, low-throughput X-ray spectra. Thus virialized gas in typical L^* galaxy’s halos can efficiently produce both O VII and N VI, but only small fractions of O VI and O VIII, the first still detectable in current FUV spectra of bright background targets.

On the contrary, PIE gas illuminated by the meta-galactic radiation can produce sizeable fractions of O VII only at typical IGM densities $n_H \lesssim 10^{-5.3} \text{ cm}^{-3}$, while O VI (and partly N VI) can still be moderately populated and detectable at typical galaxy-halo densities $n_H \simeq 10^{-4} - 10^{-5} \text{ cm}^{-3}$.

REFERENCES

Afruni, A., Fraternali, F., & Pezzulli, G. 2021, MNRAS, 501, 5575, doi: [10.1093/mnras/staa3759](https://doi.org/10.1093/mnras/staa3759)

Ahoranta, J., Finoguenov, A., Bonamente, M., et al. 2021, A&A, 656, A107, doi: [10.1051/0004-6361/202038021](https://doi.org/10.1051/0004-6361/202038021)

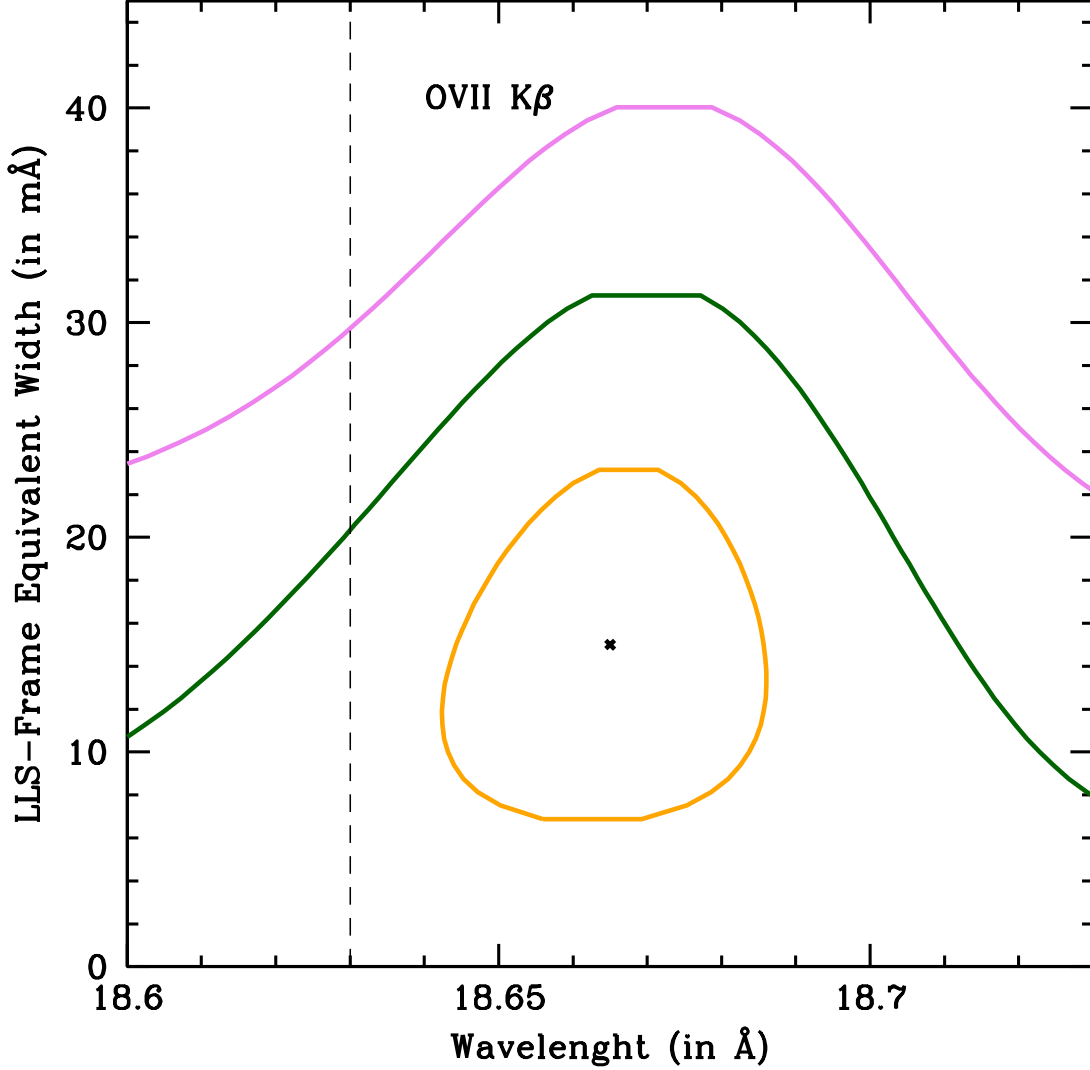


Figure 11. Orange, green and violet curves show the 1σ , 2σ , 3σ confidence levels (for one interesting parameter) in the line EW–centroid space, for the OVII $K\beta$ transition imprinted by the hot-CGM of our X-ray halo. The black cross shows the best-fitting line parameters in the LLS-frame. The best-fitting line-centroid is consistent at a 1.2σ confidence level with the rest-frame wavelength of the transition (dashed vertical line).

Ahoranta, J., Nevalainen, J., Wijers, N., et al. 2020, *A&A*, 634, A106, doi: [10.1051/0004-6361/201935846](https://doi.org/10.1051/0004-6361/201935846)
 Anders, E., & Grevesse, N. 1989, *GeoCoA*, 53, 197, doi: [10.1016/0016-7037\(89\)90286-X](https://doi.org/10.1016/0016-7037(89)90286-X)
 Armillotta, L., Fraternali, F., Werk, J. K., Prochaska, J. X., & Marinacci, F. 2017, *MNRAS*, 470, 114, doi: [10.1093/mnras/stx1239](https://doi.org/10.1093/mnras/stx1239)
 Barret, D., Lam Trong, T., den Herder, J.-W., et al. 2018, in *Society of Photo-Optical Instrumentation Engineers (SPIE) Conference Series*, Vol. 10699, *Space Telescopes and Instrumentation 2018: Ultraviolet to Gamma Ray*, ed. J.-W. A. den Herder, S. Nikzad, & K. Nakazawa, 106991G, doi: [10.1117/12.2312409](https://doi.org/10.1117/12.2312409)

Berg, M. A., Howk, J. C., Lehner, N., et al. 2019, *ApJ*, 883, 5, doi: [10.3847/1538-4357/ab378e](https://doi.org/10.3847/1538-4357/ab378e)
 Berg, M. A., Lehner, N., Howk, J. C., et al. 2023, *ApJ*, 944, 101, doi: [10.3847/1538-4357/acb047](https://doi.org/10.3847/1538-4357/acb047)
 Blackburn, J. K. 1995, in *Astronomical Society of the Pacific Conference Series*, Vol. 77, *Astronomical Data Analysis Software and Systems IV*, ed. R. A. Shaw, H. E. Payne, & J. J. E. Hayes, 367
 Bregman, J. N., Anderson, M. E., Miller, M. J., et al. 2018, *ApJ*, 862, 3, doi: [10.3847/1538-4357/aacafe](https://doi.org/10.3847/1538-4357/aacafe)
 Bregman, J. N., Hodges-Kluck, E., Qu, Z., et al. 2022, *ApJ*, 928, 14, doi: [10.3847/1538-4357/ac51de](https://doi.org/10.3847/1538-4357/ac51de)

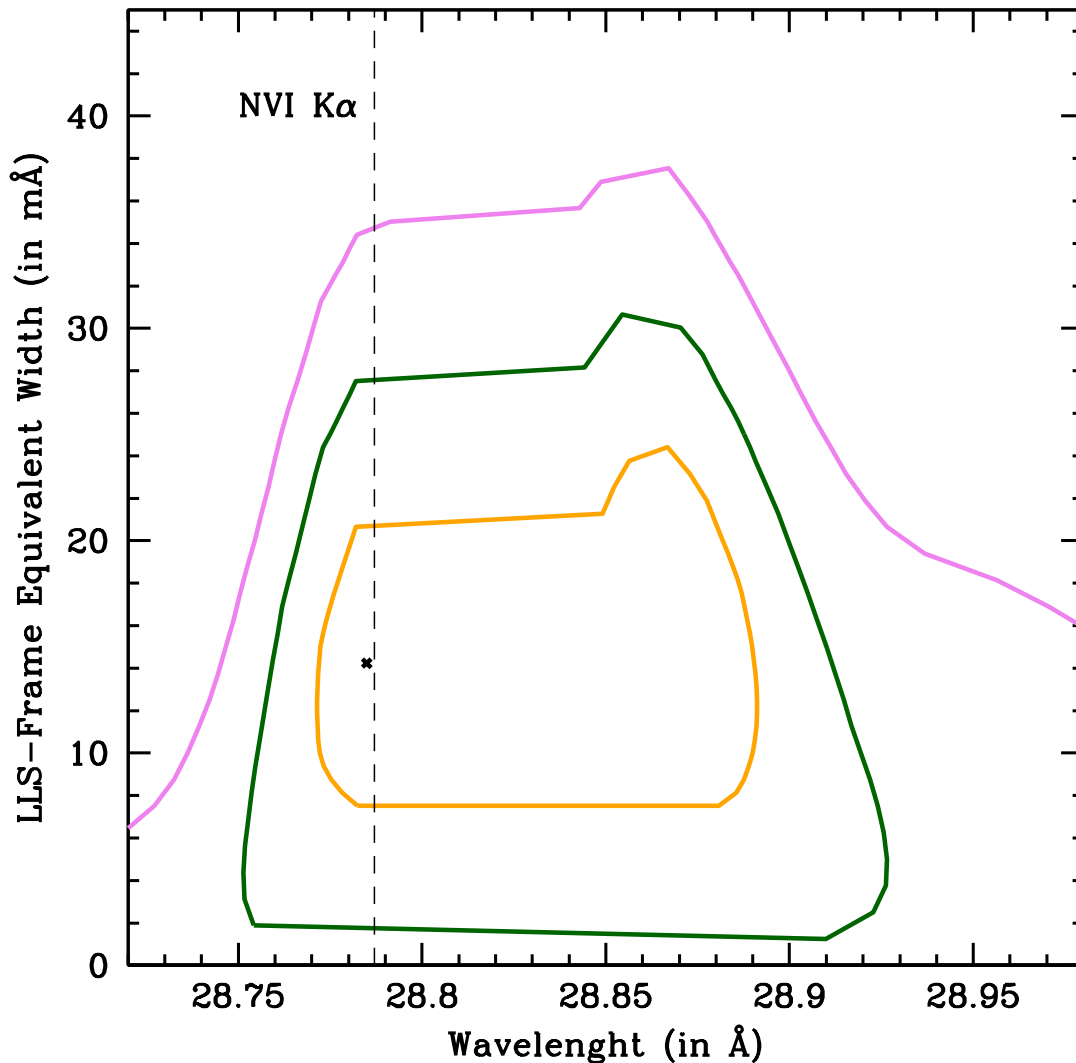


Figure 12. Same as Fig. 10, for the NVI $K\alpha$ transition imprinted by the hot-CGM of our X-ray halo. The best-fitting line-centroid is virtually coincident with the rest-frame wavelength of the transition (dashed vertical line).

Brinkman, B. C., Gunsing, T., Kaastra, J. S., et al. 2000, in Society of Photo-Optical Instrumentation Engineers (SPIE) Conference Series, Vol. 4012, X-Ray Optics, Instruments, and Missions III, ed. J. E. Truemper & B. Aschenbach, 81–90, doi: [10.1117/12.391599](https://doi.org/10.1117/12.391599)

Burchett, J. N., Tripp, T. M., Prochaska, J. X., et al. 2019, *ApJL*, 877, L20, doi: [10.3847/2041-8213/ab1f7f](https://doi.org/10.3847/2041-8213/ab1f7f)

Cavaliere, A., & Fusco-Femiano, R. 1976, *A&A*, 49, 137

Chen, H.-W., & Prochaska, J. X. 2000, *ApJL*, 543, L9, doi: [10.1086/318179](https://doi.org/10.1086/318179)

Das, S., Mathur, S., & Gupta, A. 2020, *ApJ*, 897, 63, doi: [10.3847/1538-4357/ab93d2](https://doi.org/10.3847/1538-4357/ab93d2)

den Herder, J.-W., den Boggende, A. J., Branduardi-Raymont, G., et al. 2000, in Society of Photo-Optical Instrumentation Engineers (SPIE) Conference Series, Vol. 4012, X-Ray Optics, Instruments, and Missions III, ed. J. E. Truemper & B. Aschenbach, 102–112, doi: [10.1117/12.391546](https://doi.org/10.1117/12.391546)

Fox, A. J., Lehner, N., Tumlinson, J., et al. 2013, *ApJ*, 778, 187, doi: [10.1088/0004-637X/778/2/187](https://doi.org/10.1088/0004-637X/778/2/187)

Fraternali, F. 2017, in *Astrophysics and Space Science Library*, Vol. 430, Gas Accretion onto Galaxies, ed. A. Fox & R. Davé, 323, doi: [10.1007/978-3-319-52512-9_1410.48550/arXiv.1612.00477](https://doi.org/10.1007/978-3-319-52512-9_1410.48550/arXiv.1612.00477)

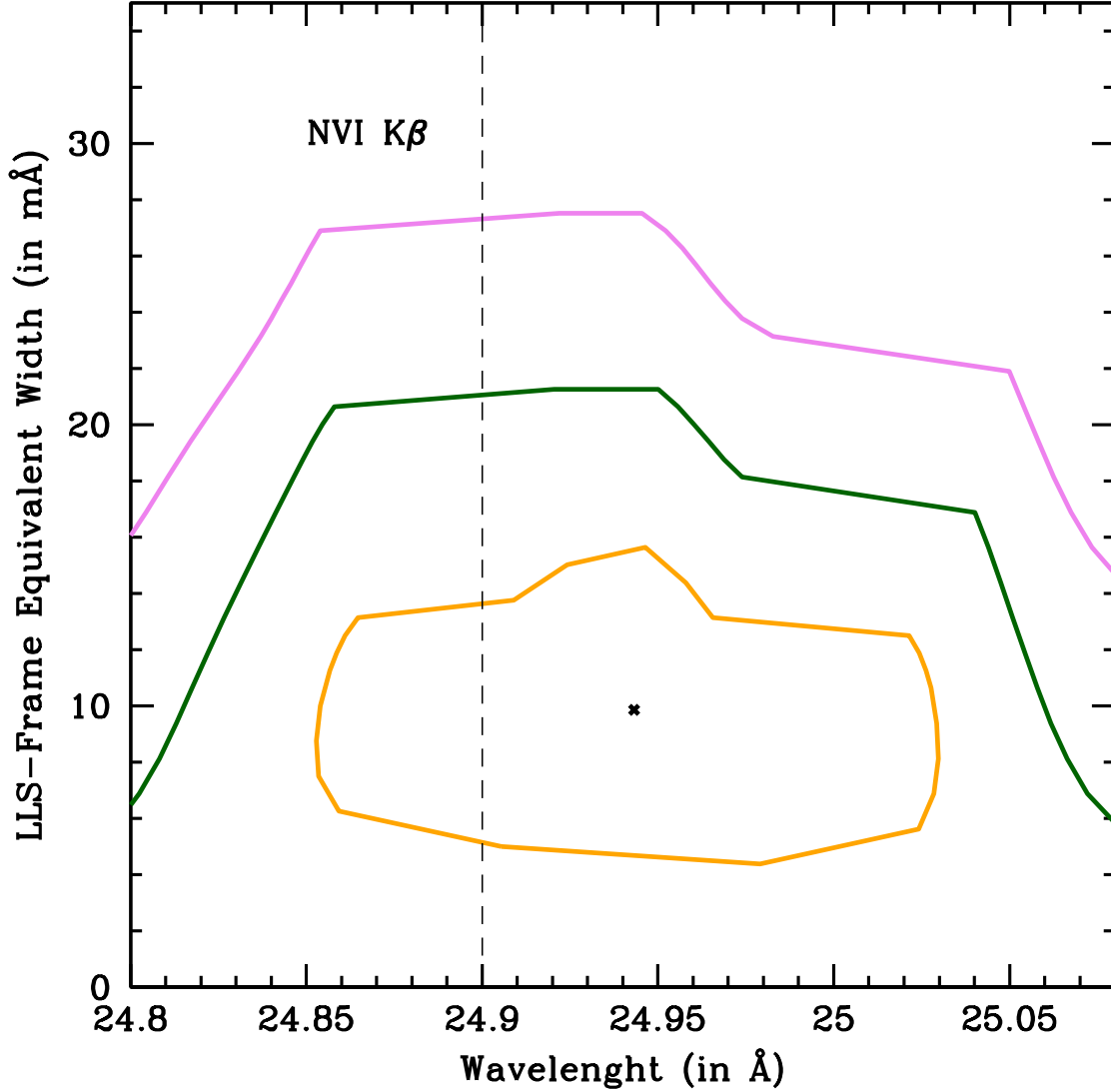


Figure 13. Same as Fig. 10, for the NVI $K\beta$ transition imprinted by the hot-CGM of our X-ray halo. The best-fitting line-centroid is consistent with the rest-frame wavelength of the transition (dashed vertical line).

Fruscione, A., McDowell, J. C., Allen, G. E., et al. 2006, in Society of Photo-Optical Instrumentation Engineers (SPIE) Conference Series, Vol. 6270, Society of Photo-Optical Instrumentation Engineers (SPIE) Conference Series, ed. D. R. Silva & R. E. Doxsey, 62701V, doi: [10.1117/12.671760](https://doi.org/10.1117/12.671760)

Gnat, O., & Sternberg, A. 2007, *ApJS*, 168, 213, doi: [10.1086/509786](https://doi.org/10.1086/509786)

Hafen, Z., Stern, J., Bullock, J., et al. 2022, *MNRAS*, 514, 5056,

doi: [10.1093/mnras/stac160310.48550/arXiv.2201.07235](https://doi.org/10.1093/mnras/stac160310.48550/arXiv.2201.07235)

Keeney, B. A., Stocke, J. T., Danforth, C. W., et al. 2017, *ApJS*, 230, 6, doi: [10.3847/1538-4365/aa6b59](https://doi.org/10.3847/1538-4365/aa6b59)

Kovács, O. E., Bogdán, Á., Smith, R. K., Kraft, R. P., & Forman, W. R. 2019, *ApJ*, 872, 83,

doi: [10.3847/1538-4357/aaef78](https://doi.org/10.3847/1538-4357/aaef78)

Lehner, N., Wotta, C. B., Howk, J. C., et al. 2018, *ApJ*, 866, 33, doi: [10.3847/1538-4357/aadd03](https://doi.org/10.3847/1538-4357/aadd03)

—. 2019, *ApJ*, 887, 5, doi: [10.3847/1538-4357/ab41fd](https://doi.org/10.3847/1538-4357/ab41fd)

Lehner, N., Howk, J. C., Tripp, T. M., et al. 2013, *ApJ*, 770, 138, doi: [10.1088/0004-637X/770/2/138](https://doi.org/10.1088/0004-637X/770/2/138)

Mathur, S., Gupta, A., Das, S., Krongold, Y., & Nicastro, F. 2021, *ApJ*, 908, 69, doi: [10.3847/1538-4357/abd03f](https://doi.org/10.3847/1538-4357/abd03f)

McGaugh, S. S., Schombert, J. M., de Blok, W. J. G., & Zagursky, M. J. 2010, *ApJL*, 708, L14,

doi: [10.1088/2041-8205/708/1/L14](https://doi.org/10.1088/2041-8205/708/1/L14)

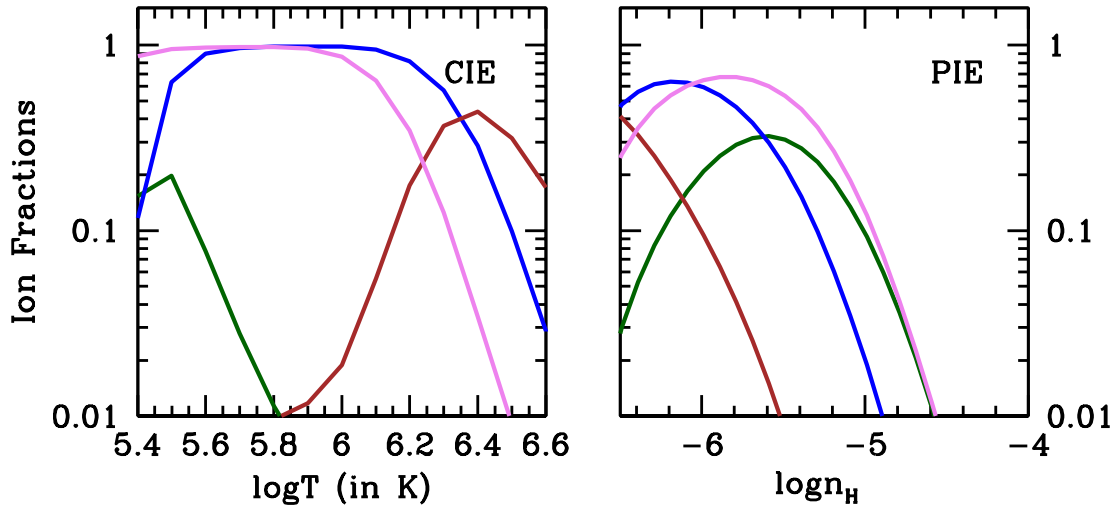


Figure 14. Fractional abundances of O VI (green), O VII (blue), O VIII (brown) and N VI (violet) as a function of temperature (left panel) and hydrogen density (right panel), in CIE (left) and PIE gas illuminated by the average meta-galactic radiation field at $z = 0.295$ (right).

- McPhate, J. B., Siegmund, O. H., Gaines, G. A., Vallerga, J. V., & Hull, J. S. 2000, in Society of Photo-Optical Instrumentation Engineers (SPIE) Conference Series, Vol. 4139, Instrumentation for UV/EUV Astronomy and Solar Missions, ed. S. Fineschi, C. M. Korendyke, O. H. Siegmund, & B. E. Woodgate, 25–33, doi: [10.1117/12.410539](https://doi.org/10.1117/12.410539)
- Murray, S. S., Austin, G. K., Chappell, J. H., et al. 2000, in Society of Photo-Optical Instrumentation Engineers (SPIE) Conference Series, Vol. 4012, X-Ray Optics, Instruments, and Missions III, ed. J. E. Truemper & B. Aschenbach, 68–80, doi: [10.1117/12.391591](https://doi.org/10.1117/12.391591)
- Nicastro, F., Senatore, F., Gupta, A., et al. 2016a, MNRAS, 457, 676, doi: [10.1093/mnras/stv2923](https://doi.org/10.1093/mnras/stv2923)
- Nicastro, F., Senatore, F., Krongold, Y., Mathur, S., & Elvis, M. 2016b, ApJL, 828, L12, doi: [10.3847/2041-8205/828/1/L12](https://doi.org/10.3847/2041-8205/828/1/L12)
- Planck Collaboration, Aghanim, N., Akrami, Y., et al. 2020, A&A, 641, A6, doi: [10.1051/0004-6361/201833910](https://doi.org/10.1051/0004-6361/201833910)
- Prochaska, J. X., Weiner, B., Chen, H. W., Mulchaey, J., & Cooksey, K. 2011, ApJ, 740, 91, doi: [10.1088/0004-637X/740/2/91](https://doi.org/10.1088/0004-637X/740/2/91)
- Prochaska, J. X., Burchett, J. N., Tripp, T. M., et al. 2019, ApJS, 243, 24, doi: [10.3847/1538-4365/ab2b9a](https://doi.org/10.3847/1538-4365/ab2b9a)
- Qu, Z., & Bregman, J. N. 2018, ApJ, 856, 5, doi: [10.3847/1538-4357/aaafd4](https://doi.org/10.3847/1538-4357/aaafd4)
- Rodríguez-Puebla, A., Primack, J. R., Avila-Reese, V., & Faber, S. M. 2017, Monthly Notices of the Royal Astronomical Society, 470, 651, doi: [10.1093/mnras/stx1172](https://doi.org/10.1093/mnras/stx1172)
- Savage, B. D., Narayanan, A., Wakker, B. P., et al. 2010, ApJ, 719, 1526, doi: [10.1088/0004-637X/719/2/1526](https://doi.org/10.1088/0004-637X/719/2/1526)
- Smith, R. K. 2020, in Society of Photo-Optical Instrumentation Engineers (SPIE) Conference Series, Vol. 11444, Society of Photo-Optical Instrumentation Engineers (SPIE) Conference Series, 114442C, doi: [10.1117/12.2576047](https://doi.org/10.1117/12.2576047)
- Stocke, J. T., Keeney, B. A., Danforth, C. W., et al. 2013, ApJ, 763, 148, doi: [10.1088/0004-637X/763/2/148](https://doi.org/10.1088/0004-637X/763/2/148)
- Tchernyshyov, K., Werk, J. K., Wilde, M. C., et al. 2022, ApJ, 927, 147, doi: [10.3847/1538-4357/ac450c](https://doi.org/10.3847/1538-4357/ac450c)
- Tumlinson, J., Thom, C., Werk, J. K., et al. 2011, Science, 334, 948, doi: [10.1126/science.1209840](https://doi.org/10.1126/science.1209840)
- van de Voort, F., & Schaye, J. 2012, MNRAS, 423, 2991, doi: [10.1111/j.1365-2966.2012.20949.x](https://doi.org/10.1111/j.1365-2966.2012.20949.x)[10.48550/arXiv.1111.5039](https://arxiv.org/abs/10.48550/arXiv.1111.5039)
- Werk, J. K., Prochaska, J. X., Thom, C., et al. 2013, ApJS, 204, 17, doi: [10.1088/0067-0049/204/2/17](https://doi.org/10.1088/0067-0049/204/2/17)
- Werk, J. K., Prochaska, J. X., Tumlinson, J., et al. 2014, ApJ, 792, 8, doi: [10.1088/0004-637X/792/1/8](https://doi.org/10.1088/0004-637X/792/1/8)
- Wijers, N. A., Schaye, J., & Oppenheimer, B. D. 2020, MNRAS, 498, 574, doi: [10.1093/mnras/staa2456](https://doi.org/10.1093/mnras/staa2456)
- Wotta, C. B., Lehner, N., Howk, J. C., et al. 2019, ApJ, 872, 81, doi: [10.3847/1538-4357/aafb74](https://doi.org/10.3847/1538-4357/aafb74)

Yao, Y., Wang, Q. D., Penton, S. V., et al. 2010, ApJ, 716,
1514, doi: [10.1088/0004-637X/716/2/1514](https://doi.org/10.1088/0004-637X/716/2/1514)